nature catalysis

Article

https://doi.org/10.1038/s41929-023-00983-8

Dynamic and reversible transformations of subnanometre-sized palladium on ceria for efficient methane removal

In the format provided by the authors and unedited

This PDF file includes:

Supplementary Methods
Supplementary Notes 1 to 5
Supplementary Figs. 1 to 30
Supplementary Tables 1 to 8
Supplementary References 1 to 48

Supplementary Methods

Chemicals and Catalyst Synthesis

All the chemicals are used as received from the provider without further purification. Tetraamminepalladium (II) nitrate solution (TAPN, 10 wt. % in H_2O, 99.99 %) and Cerium (III) nitrate hexahydrate ($Ce(NO_3)_3 \cdot 6H_2O$, 99.995 %) obtained from Sigma Aldrich were used as the precursors of Pd and CeO_2, respectively. Gamma phase of aluminum oxide (CATALOX SBa-150) from Sasol was pre-calcined at 850 ^oC in air for 6 hours and used as the reference catalyst support.

Pd_1/CeO_2. Single-atom Pd/CeO_2 was prepared *via* incipient wetness impregnation followed by high-temperature calcination as reported previously. Firstly, CeO_2 support with mild-crystallinity was obtained via thermal decomposition of $Ce(NO_3)_3 \cdot 6H_2O$ at 350 ^oC in air for 2 h. After impregnation of TAPN (1 wt. % Pd), the powders were dried overnight at 80 ^oC followed by calcination in static air at 800 ^oC for 8 h with a ramp of 5 ^oC min^{-1}. The resulted catalyst was denoted as Pd_1/CeO_2.

PdO/Al_2O_3. Traditional Pd/Al_2O_3 catalyst dominated by supported PdO NPs was prepared by impregnating commercial γ-Al_2O_3 with TAPN (1 wt. % Pd), drying the impregnated support in air at 80 ^oC, and calcining the powders in static air at 550 ^oC for 5 h with a ramp of 5 ^oC min^{-1}. The resulted catalyst was denoted as PdO/Al_2O_3.

Materials Characterization

X-ray diffraction (XRD) measurements were conducted on a Rigaku SmartLab with the 2 Theta from 15 ° and 85 °, using a scanning rate of 1 °/min at a step of 0.01°. The employed radiation was Cu K-α with a wavelength of 0.154 nm. Additional high energy x-ray diffraction and pair distribution function studies have been conducted in the beamline 11-ID-C at Advanced Photon Source (Argonne National laboratory). The Brunauer, Emmett and Teller (BET) surface areas were determined by a Micromeritics TriStar II 3020 using N_2 adsorption at -196 ^oC. The visible (532 nm) Raman spectra were collected at room temperature (RT) using a Horiba LabRAM HR Raman microscope equipped with a Synapse Charge Coupled Device (CCD) camera and an *in situ* sample cell (Linkam CCR 1000).

Electron Spectroscopy

Transmission electron microscopy (TEM) images were taken using a FEI Titan 80-300^{TM} at 300 kV. Subsequent image analysis and processing were carried out using the Gatan DigitalMicrograh® software. Sample preparation involved an initial meshing through a 100 mesh No. grid. Then, a small amount of powder was thoroughly dissolved in ethanol and further deposited on a 200 mesh Lacey Carbon Cu grid, where the ethanol was fully evaporated before imaging.

X-ray Absorption Spectroscopy (XAS)

X-ray absorption near edge structure (XANES) and extended X-ray absorption fine structure (EXAFS) measurements at Pd K-edges were carried out twice at beamlines 20-BM and 20-ID in Advanced Photon Source (Argonne National laboratory). The catalyst powders after reactions were collected and made into pellets, and then brought to beamline for measurement in fluorescence mode. Photon energies were selected using a Si (111) monochromator, which was detuned to reduce the harmonic reflections. Standard procedures for the normalization and background subtraction were performed using the Demeter 0.9.25 software package. The edge energy of the XANES spectrum was determined from the inflection point in the leading edge, that

is, the maximum in the first derivative of the leading edge of the XANES spectra. The structural parameters were obtained by a least-squares fit in R space for the k^3-weighted Fourier transformed data using Artemis[1]. The amplitude reduction factor in these measurements was determined by the EXAFS fitting of the Pd foil that was measured simultaneously with the sample in transmission mode during the experiments.

Activity Measurements

Catalytic CH_4 combustion over the above catalysts were conducted using a fixed bed flow reactor. 60 mg of catalyst powders (150 μm) diluted by 1500 mg SiC was packed inside a quartz tube (I.D. 1/2 inch) with coarse frit (40-100 μm) in the middle. The reaction was performed at atmospheric pressure. Dry reaction gas consisted of 680 ppm CH_4, 5 vol % CO_2 and 14 vol % O_2 balanced with N_2 with a total flow of 300 ml min^{-1}, and a gas hourly space velocity (GHSV) of 300,000 ml g^{-1} h^{-1}. Different amounts of H_2O vapor (0-10 vol %) was introduced into the reaction gas by an in-line temperature-controlled stainless-steel bubbler. Before evaluating the performance, all catalysts were pre-activated by heating up to 800 ^oC in 14 % O_2/N_2 or in dry reaction gas. This pre-treatment also removed adsorbates on catalyst surface. During the measurements, the effluent gas was analyzed by an online continuous FTIR MKS MultiGas™ Analyzer equipped with a LN-cooled MCT detector. For light-off tests, catalysts were heated with a ramp of 5 ^oC/min in reaction gas and cooled down to room temperature in 14 % O_2/N_2 before the next run. In addition to the light-off activities, time-on-stream (TOS) stabilities of catalysts were also tested under isothermal conditions. For each catalyst, additional pre-treatments were also employed to simulate different surface status of supported Pd species.

RT-CO. The catalysts were treated at room temperature (RT) in 2 % CO, 14 % O_2, balanced with N_2 with a total flow of 150 ml min^{-1} for 5 min. Different treatment time other than 5 min were also employed and indicated in the discussion. For comparison, the treatment was also repeated in 2 % CO/N_2 or 2 % CO added to the dry reaction stream.

275-CO. The catalysts were heated to 275 ^oC in N_2, reduced in 2 % CO/N_2 with a flow rate of 150 ml min^{-1}, and cooled down to RT in N_2 before introducing reaction gas for performance evaluation.

HTA (hydrothermal aging). The catalysts were heated to 750 ^oC in the stream consisting of 14 % O_2/N_2 with the total flow of 150 sccm. At 750 ^oC, 10 % H_2O was introduced into the stream and held for 9 hours to age the catalysts. Afterwards, H_2O was stopped, and temperature was held at 750 ^oC for another 30 min before cooling the catalyst bed down to room temperature in the same O_2/N_2 atmosphere.

Diffuse Reflectance Infrared Fourier Transform Spectroscopy (DRIFTS)

The RT-CO and 275-CO treatments of Pd_1/CeO_2 catalyst were monitored using *in situ* infrared spectroscopy in the diffuse reflectance mode on a Tensor 27 spectrometer (Bruker) equipped with a DRIFTS cell (Harrick Scientific Inc.). The catalyst powders were loaded in the DRIFTS cell and pre-treated at 400 ^oC in 10 % O_2 for 30 min. Afterwards, the sample cell was cooled down to RT and the background spectrum was collected. For both RT-CO, 2 % CO, 8 % O_2, balanced with He with a total flow of 100 ml min^{-1} was employed. For 275-CO, 2 % CO/He (100 ml min^{-1}) was employed. IR spectra were recorded every 1 min during the treatments.

O_2 Temperature-Programmed Oxidation (O_2-TPO)

O_2-TPO experiments were conducted on the Autochem 2920 (Micromeritics). The catalyst powders (60 mg) were placed in a U-shaped quartz reactor and pre-calcined to 800 ^oC in 10 % O_2. TPO measurements were carried out in 2 % O_2 balanced with 5 % Ar/He (60 ml min^{-1}) by increasing the temperature from RT to 900 ^oC with a ramp of 10 ^oC min^{-1}, followed by cooling down to 300 ^oC in the same gas. Oxygen release-uptake during the heating/cooling processes was recorded using a QMS equipped with a Secondary Electron Multiplier detector. Ar signal was used as an internal standard to normalize the other signals. For Pd_1/CeO_2 catalyst, the above TPO measurements were also repeatedly performed after the RT-CO pre-treatment to verify the regeneration of single-atom catalyst.

Atomic Models for Computational Studies

Models of the Pd/CeO_2 catalysts surface were created to mimic representative catalyst motifs for terrace and stepped sites using the Atomic Simulation Environment (ASE) software suite[2].

A Pd-doped terrace site model was generated by replacing one Ce with Pd for the most common (based on STEM images)[3] and lowest energy surface facet, CeO_2 (111)[4,5]. This is equivalent to a model proposed by Su et al. and reported frequently in the literature for Pd and for other dopants such as Au, Cu, and Pt[6-10]. As discussed in the computational results (Supplementary Note 1), the geometry and bond distances of the optimized low energy Pd_1 and Pd_2 structures for this model agrees well with the EXAFS results (Supplementary Table 5). The model comprises a three CeO_2 layer thick (i.e., nine atomic layers) 3 × 3 surface super cell with the dimensions 11.64 × 11.64 $Å^2$, created from an optimized cubic CeO_2 bulk fluorite structure (a = 5.485 Å, within 1.4 % variation of the experimental lattice constant[11]). The top two CeO_2 layers (i.e., six atomic layers) of the surface model were free to relax and the remaining atoms kept fixed at their lattice positions. Substituting one Ce in the model for Pd gives a Pd surface coverage of ~1 nm^{-2}, which is approximately the same as the experimental loading. In the low energy structure, the doped Pd breaks the 3-fold symmetry of the center at the Ce-vacancy site and relaxes to one of the sides assuming a square-planar Pd_1O_4 structure. For the V_O (oxygen vacancy) calculations, the results were compared to a 4 × 4 surface super cell to evaluate convergence with respect to O-Pd distance.

Stepped sites of the step-II kind[9,12,13] (also known as U-step[14]) were modeled by epitaxial addition of a 3 × 2 semi-layer of CeO_2 on top of a 3 × 4 surface super cell of CeO_2 (111). This step structure is equivalent to the steps on a CeO_2 (311) surface and has been attributed special importance in previous work of CeO_2 single-atom catalysts[12,14,15]. However, these sites would not be sufficiently abundant to fully account for the loading of the dispersed Pd_1 single-atom catalysts used in this study. Compared to the step-II* structure, where the topmost O resides in 3-fold hollow Ce step sites, the step-II surface has the top O layer coordinated above Ce at Ce-Ce bridges[13]. In this model, the thermodynamically favored Pd/CeO_2 structure at synthesis conditions contains Pd + O_2(g) co-adsorbed in-between the topmost and second O layers with the O_2 dissociatively adsorbed flanking each side of Pt yielding a square-planar Pd_1O_4 structure.

In addition to the Pd single atom systems, PdO_x SNCs structures were also considered on the above surface models. For the terrace site model, low energy dimer and trimer Pd structures were optimized whereas, for the stepped site model, only dimer structures were optimized. In addition, Pd ad-atom states as well as states with CO adsorbed were included in the analysis. Finally, low energy states with $\pm n$ oxygen atoms (n ranging from 1 to 3 if applicable) per unit cell were identified to allow evaluation of the thermodynamically favored reduced/oxidized state at the various conditions considered.

To ensure that we compare the terrace and step sites on an equal footing, we evaluate the energetics of the various PdO_x SNCs states on an enlarged 3 × 6 surface step model and relate this to the results from the smaller models. On top of this 3 CeO_2 layer thick model, a 3 × 2 semi-layer of CeO_2 was added in epitaxial position. The added semi-layer represents steps and the remaining 3 × 4 of the surfaces represent the terrace. The model leaves sufficient space to simultaneously consider Pd adsorbed on the step edge and Pd doping on a terrace site.

Gas phase molecules (CO, CO_2, and O_2, as well as atomic Pd) were modeled in a 21×22×23 $Å^3$ cell. Bulk calculations of Pd(s), PdO(s) and CeO_2(s) were carried out using their respective unit cells.

All optimized structure and corresponding 0 K energetics are uploaded to the open data base catalysis-hub.org via the link https://www.catalysis-hub.org/publications/JiangDynamic2023. Note that, for technical reasons, in the Catalysis-hub repository all palladium adsorption energies are reported relative to gas phase palladium, Pd(g). To convert to energies relative to solid palladium, Pd(s), which is the reference used in this manuscript, the DFT-computed atomization energy E_{atom} = 3.74(2) eV should be added to the adsorption energies reported at Catalysis-hub. Note, in addition, that the reported energies in Catalysis-hub do not contain the gas phase energy corrections for O_2, CO, and CO_2 explained below.

Density Functional Theory Calculations

Periodic and spin-polarized density functional theory (DFT) calculations were performed using the Vienna Ab-initio Simulation Package (VASP, version 5.4.4)[16,17] and the Perdew-Burke-Ernzerhof (PBE) functional[18]. Hubbard corrections[19] were applied to the Ce 4*f* states using a U_{eff} of 4.5 eV, as suggested by Fabris et al.[20] The electronic valence states–Ce(5s,5p,6s,4f,5d), Pd(4d5s), O(2s,2p), and C(2s,2p)–were expanded on plane-wave basis sets with a 400 eV cut-off for the surface, gas phase, and final bulk energy calculations. The bulk structures were optimized using an 800-eV basis set. Core states were represented by projector augmented wave (PAW) method potentials[21,22]. The Brillouin zone was sampled on Γ-centered Monkhorst-Pack type[23] 3×3×1, 3×2×1, 3×1×1, 2×2×1 **k**-point grid for the 3×3, 3×4, 3×6, 4×4 surface super cell models, respectively, a 11×11×11 grid for the bulk calculations, and a 1×1×1 grid for the gas phase molecules. A Gaussian smearing with a sigma value of 0.1 eV was applied. Convergence was set to 10^{-5} eV and 0.03 eV $Å^{-1}$ for the electronic and geometric relaxation, respectively. For the thermochemical analysis, tighter convergence criteria of 10^{-6} eV and 0.01 eV $Å^{-1}$ were used to ensure well converged forces. A vacuum of at least 15 Å between repeating slab images was employed in order to avoid spurious interactions between slabs. The results compare well to calculations using dipole corrections affirming convergence with vacuum distance. To correct for known issues in describing gas phase energetics with generalized gradient approximation DFT (e.g., the PBE functional used herein), established corrections were applied to the O_2 (0.67 eV), CO (-0.51 eV), and CO_2 (0.13 eV) gas phase energies[24]. These corrections ensure the correct energetics of, e.g., the $CO(g) + ½O_2(g) \rightarrow CO_2(g)$ reaction.

Thermochemical Analysis

Thermochemical data for the surface and gas-phase states was obtained from vibrational analysis and from the NIST-JANAF database[25]. Numerical vibrational analyses were performed on optimized structures using the harmonic oscillator and central difference approximation by ±0.015 Å displacements of the unconstrained atoms. Only thermochemical contributions from the vibrational modes were considered for the slab and bulk states, whereas for the gas phase

molecules vibrational, rotational, and translational contributions were accounted for using, in addition to the harmonic oscillator, the rigid rotor and ideal gas approximations. Thermochemical data at 298 K, 923 K, and 1073 K was extracted via the Vaspkit software[26]. The chemical potential, μ_i, of a state, *i*, at a given condition (temperature *T* and pressure p_i) is computed as:

$$\mu_i(T,p_i) = E_{DFT} + ZPE + \int C_p(T)dT - TS(T,p_0) - k_B T\ln(p_i/p_0) \quad \text{Supplementary Equation (1)}$$

where E_{DFT} is the raw PBE+*U* energy computed by the ab initio program with gas-phase energy corrections added. Zero-point energy, ZPE, enthalpy, $\int C_p(T)dT$, and entropy, $TS(T,p_0)$, corrections come from the numerical vibrational analysis with values for gas-phase molecules matching experimental values in the NIST-Janaf database within 0.01 eV. The $k_BT\ln(p_i/p_0)$ term corrects to an arbitrary pressure from the reference pressure, p_0, of 1 bar.

The relative chemical potential (i.e., Gibbs free energy, $\Delta G_i = \Delta\mu_i$) for a chemical transformation is given by:

$$\Delta\mu_i = \Sigma\mu_{products} - \Sigma\mu_{reactants} \quad \text{Supplementary Equation (2)}$$

The thermochemical data used is summarized in Supplementary Table 4.

Supplementary Notes

Supplementary Note 1

(Pd/CeO_2 models)

As described in the computational details section, two types of smaller models were created to represent the most plausible environment(s) for Pd on the CeO_2 catalysts support. Another, extended model was also constructed that encompassed both of the models above in one single model. The first of the smaller models was designed to represent the flat terrace surfaces of the most stable and most common CeO_2(111) facet. Previous studies have suggested a Pd-doped surface with one Pd directly replacing one Ce[7]. The second of the smaller models was created to mimic step sites that will inevitably be present on the surface. Here we employed a model representing the so-called step-II (or U-step) step between two (111) facets. This is also a common model frequently used in the literature[12,14,15]. The energetics of Pd in different states on these models are discussed in a later section. Below, we discuss the structural features of the models in comparison to experimental EXAFS results.

In the lowest energy state of both the terrace and step models (at synthesis condition, i.e., *T*=1073 K, p_{CO}= p_{CO2}=0.0 bar, and p_{O2}=0.2 bar), Pd relaxes to a square planar structure coordinated to four O, and with four Ce atoms in the extended nearest coordination sphere (Supplementary Fig. 26). As seen in Supplementary Table 5, both models yield coordination environments around Pd that, given the inherent uncertainties in both DFT and experiments, reasonably (within ±0.1 Å) reproduces bond-distances estimated from the EXAFS data for Pd/CeO_2 prior to exposure to CO. In particular, the coordination number (CN) for Pd-O (CN=4), Pd-Pd (CN=0), and Pd-Ce (CN=4) estimated by EXAFS is identical to the CNs in the lowest energy DFT-structures. It should be noted that for both the step and terrace models, the correspondence between the experimental and DFT bond-distances is enhanced if the stoichiometric (for the step model, stoichiometric plus PdO_2) surface is mildly reduced by extraction of a O attached to Ce but not to Pd (i.e., the least

stable O site), see Supplementary Table 5. Although currently inconclusive, this could suggest that the as-synthesized Pd/CeO_2 surface has a certain amount of O vacancies.

Upon formation of Pd_2 dimers (i.e., PdO_x SNCs) on the surface, the $CeO_2(111)$ terrace site stands out as a more plausible alternative to the step sites when comparing to experimental data. Experimentally, the EXAFS data clearly suggests a short Pd-Pd bond of around 2.72 Å. The lowest energy Pd dimer structure on the step site model has a bridging O in between the Pd atoms, resulting in a much too long Pd-Pd distance of 3.89 Å. Efforts to identify structures with a direct Pd-Pd bond at the step, always results in the spontaneous separation of the Pd into distinct ad-atoms. The same result is found for Pd atoms adsorbed directly on the terrace surface, i.e., if neither of the Pd atoms are located at a Ce vacancy (thus, in this case we have no surface doping). On the Pd-doped terrace site, on the other hand, the Pd atoms instead prefer to bind at a distance of 2.77 Å, which closely resembles the experimental value. Although, for both the terrace and step models, the Pd-O distances are in good agreement with EXAFS data, the Pd-Ce distances of the terrace model are in close agreement with the experimental data in contrast to the considerably longer bonds on the step site model.

Supplementary Note 2

Oxygen extraction and (re)adsorption

The favored coverage of oxygen under various conditions is established for Pd at different states including single atom (Pd_1), dimer and trimer nanoclusters (Pd_2, Pd_3), as well as for Pd ad-atom states (Pd_{ad}). At high temperature (800 ^oC) and 0.2 bar $O_2(g)$ corresponding to the catalysts synthesis conditions, single atom Pd_1 coordinated to four O (yielding $Pd^{\sim 2+}$) is the favored state on both the terrace and step model surface, see, e.g., Fig. 4. For the stepped surface, this corresponds to the adsorption of one unit of PdO_2 (i.e., $Pd+O_2(g)$) relative to the stoichiometric surface. It is found that the introduction of the adsorbed PdO_2 weakens the binding energy of a nearby lattice oxygen at the step-edge. In fact, the most favored surface state under synthesis conditions includes a V_O at that site. Supplementary Fig. 27 provides an overview of the herein considered structures for the stoichiometric and reduced states of Pd. Supplementary Fig. 28 compares the favored surface oxidation state at different conditions and illustrate the binding energy difference for O atoms on the surface in relation to their position with respect to Pd_1.

Upon introduction of CO(g) (0.02 bar at 25˚C), both the DFT and experimental results suggests that the surface can be reduced trough mild oxygen extraction via

$$CO(g) + O_{surface} \rightarrow CO_2(g) + V_O \qquad \text{Supplementary Equation (3)}$$

leaving oxygen vacancies (V_O) behind. The pristine $CeO_2(111)$ surface is not very prone to reduction (by CO) with a Gibbs free energy of oxygen extraction, $\Delta G(V_O)$, of -0.2 eV. Pd_1 greatly enhances the reducibility of the surface via Pd-doping of the terrace and PdO_2 adsorption on the stepped $CeO_2(111)$ surface. Supplementary Figs. 28a and 28b show the oxygen extraction results as a function of distance to the Pd site on the $CeO_2(111)$ terrace surface. Supplementary Fig. 28c shows the corresponding data for the step site model. For both models, undercoordinated oxygen atoms close to, but not directly bond to, the Pd_1O_4 site have the most favorable energetics for extraction. These are the oxygen at the Ce vacancy for the terrace site and at the step edge for the step site. It is, however, clear that Pd_1 generally enhances the reducibility of the surface also for distant sites. In contracts, relative to the surface oxygen, the oxygen at Pd_1O_4 is not easily extracted; for the terrace site, e.g., the surface spontaneously reconstructs to regenerate Pd_1O_4 via

the migration of a subsurface atom (site B in Supplementary Fig. 28a) if the topmost oxygen of Pd_1O_4 is removed.

Two to three oxygen per Pd can be extracted from the surface (i.e., two to three oxygen per nm^2) by CO at 298 K for both the terrace and step model relative to the thermodynamically favored state at synthesis conditions (T=1073 K, p_{CO}= p_{CO2}=0 bar, and p_{O2}=0.2 bar). For the terrace model, two oxygen atoms are extracted from the rim of the Ce vacancy that are not bonded to Pd. A Pd_1O_3 state can be generated via the influence of co-adsorbed CO as described in the next section without the extraction of additional oxygen. The step site can also be reduced, and in this case, three oxygen atoms can be removed, two directly attached to the adsorbed Pd and one at an adjacent step-edge site, resulting in a Pd_1O_2 unit adsorbed at a reduced II-step. See Supplementary Tables 6, 7, and 8 for more detailed energetics.

In the process of growing PdO_x SNCs, it is expected that Pd_{ad} forms from the least stable Pd_1 sites. Thus, forming the ad-atom state will define the barrier for PdO_x SNCs formation. These Pd_{ad} will migrate over the surface generating dimers, trimers, et cetera, with neighboring Pd sites. CO plays a crucial role in activating the mobility of Pd on the surface via two mechanisms: i) surface reduction that destabilizes Pd_1, and ii) assisting Pd_{ad} and stabilizing the nanoclusters through non-reductive CO adsorption. The latter is discussed in the next section.

The results of our DFT simulations, comprised in Supplementary Table 8, suggest that an additional oxygen atom can be extracted per nm^2 from the Ce vacancy site of the surface upon formation of Pd_{ad} from Pd_1. Once dimer and trimer clusters are formed, however, the surface reducibility around the nanocluster site is decreased. One may also ask the question if the nanoclusters or the intermediate states at the surface can be reoxidized (from a surface state with two O extracted per nm^2) by the $CO/CO_2/O_2$ gas mixture upon their formation? While this does not appear to be the case for either of the states Pd_{ad} and Pd_2 (and Pd_1 as discussed previously), oxidation of Pd_3 is exergonic (-0.17 eV) up to one O per nm^2. However, this will compete with adsorption of a second CO onto Pd_3, as described below, which is more favorable (-0.63 eV).

Supplementary Note 3

CO adsorption and Pd mobility

Supplementary Fig. 29 summarizes the adsorption energies for CO on the considered Pd structures. CO adsorption is generally exergonic on Pd in its various states at the $CeO_2(111)$ surface at 298 K and 0.02 bar p_{CO}. The weakest interaction of CO is with the Pd_1 single atom state of the terrace model. While the interaction becomes more favorable as the site and the nearby surface is reduced, the difference in CO adsorption strength onto Pd_1 compared to adsorbed Pd (Pd_{ad}) and Pd in PdO_x nanoclusters (Pd_2-Pd_3) helps rationalize the behavior of Pd upon CO adsorption and the accompanying tendency towards cluster formation.

In brief, we find that the total effect of exposure to CO at room temperature leads to the activation of Pd_1 at step sites, i.e., the least stable site. In contrast to doped Pd_1 at terrace sites that remain stationary, the step-site Pd_1 becomes mobilized and diffuses, facilitated by adsorbed CO, on the surface until encountering a terrace-residing Pd_1, with which dimer (and eventually trimer et cetera) PdO_x SNCs are formed. The process is reversible at increased temperature (923 K) and CO lean conditions. A more detailed account follows below.

For a $Pd_1/CeO_2(111)$ surface (step and terrace) without oxygen vacancies (V_O), CO interaction at around Pd_1 leads to the spontaneous reduction of the nearby surface and desorption of CO_2 as described in the section above. The same reoccurs until approximately two-three oxygen per nm^2 has been extracted. This process leaves behind a square-planar Pd_1O_4 unit in a reduced

environment on the terrace sites, and a linear Pd_1O_2 on the steps. Further reduction of the terrace site leading to Pd_1O_3 is slightly endergonic (0.44 eV), and so is CO adsorption onto this Pd state (0.28 eV). However, if CO adsorbs onto Pd_1O_4, creation of Pd_1O_3 can be achieved through an essentially thermoneutral (ΔG_{ad}=0.01 eV) swap between CO adsorbed at a nearby CeO site and the topmost O of Pd_1O_4:

$$CO\text{-}CeO + Pd_1O_4 \leftrightarrow CeO_2 + CO\text{-}Pd_1O_3 \qquad \text{Supplementary Equation (3)}$$

In as-formed CO-Pd_1O_3, Pd detaches from the rim of Ce vacancy site and sits in a square-planar configuration centrally in the site with CO as the topmost ligand. From this state, Pd_{ad} could be formed through a mildly endergonic process (0.65 eV). This state can either return to Pd_1 in the Ce vacancy, or migrate over the surface and form PdO_x SNCs with nearby Pd. Nevertheless, the formation of, e.g., a PdO_x dimer is endergonic by 0.5 eV compared to Pd_1. In other words, still energetically uphill and disfavored.

Although the above energy analysis clearly demonstrated that CO could activate Pd and bring the Pd_1 state closer to the chemical potential of other Pd states such as dimer and trimer SNCs, it does not offer a full explanation of the formation of the experimentally observed PdO_x SNCs on the surface. Instead, Pd atoms attached at surface steps provide a more plausible source of Pd for the PdO_x SNCs. These step-residing Pd_1 are readily reduced leading to an activated Pd_1 state that is energetically disfavored compared to PdO_x SNCs; the formation of a Pd_2 dimer SNCs is downhill by -0.20 eV (Figs. 4b and 4c, and Supplementary Fig. 29).

When CO interacts with Pd_1 at step sites, the Pd_1O_4 is reduced to Pd_1O_2. CO adsorbs strongly (ΔG_{ad}=-0.96 eV) on this Pd state forming a linear CO-Pd-O structure with Pd detached from the step. Here the combined reduction of the site by CO and subsequent CO adsorption significantly enhances the mobility of Pd ad-atoms at step sites. Similarly, CO facilitates Pd-diffusion between the step and terrace sites as shown in Fig. 4c. CO destabilizes the single atom (Pd_1) terrace sites. However, the exergonic CO adsorption onto Pd ad-atoms (Pd_{ad}) close to the step edge (-0.85 eV) and at Pd_{ad} the CeO_2(111) surface (-0.73 eV), as well as onto reduced PdO_x dimer and trimer sites (Pd_2 and Pd_3), facilitates the migration of Pd atoms over the surface and growth of PdO_x nanoclusters. The dimer structure anchored at Pd-doped terrace sites, adsorbs one CO, at the Pd-Pd bridge site, per cluster (ΔG_{ad}=-0.89 eV). The larger trimer nanocluster can harbor two CO; whereas the first CO adsorbs at a bridge site between the two topmost Pd atoms (ΔG_{ad}=-1.50 eV), the second CO resides on top of the very topmost Pd (ΔG_{ad}=-0.46 eV) forming a 104˚ (C-Pd-C) angle with the Pd adsorption site and the first adsorbed CO. Compared to dimer structures anchored by Pd-doping at a Ce vacant terrace site, surface Pd_2 ad-atom clusters are not favorable and falls apart into two Pd_{ad} during structure optimization.

While it should be noted that the computational results on its own merely suggest an atomistic picture for the formation of terrace PdO_x SNCs upon interaction with CO, together with the experimental data it provides a tenable rationale for the observed catalytic behavior and reversible generation of active sites on the Pd/CeO_2 system. Our simulation results suggest that Pd_1 at step surfaces become mobilized and migrate on the surface upon CO exposure until forming PdO_x nanoclusters. Thus, all in all, Pd residing in strongly interacting terrace site(s) remain immobilized serving as nucleation site(s) for mobilized Pd originating from less stable step sites, and possibly from other defect sites.

Supplementary Note 4

Thermochemistry at varied conditions

The thermodynamics of Pd in various states on terrace and stepped sites of CeO_2(111) are shown in Supplementary Fig. 30 under different conditions. This figure is an extension of Fig. 4b including a larger number of states. All in all, the exposure to CO has the effect of bringing the chemical potential of Pd in various states closer. In particular, the large preference for dispersed Pd_1 single-atoms at the CO lean, O_2 rich, and high-temperature synthesis conditions is leveled out when CO is introduced at room temperature (25 ˚C) favoring the nucleation and growth of larger PdO_x nanoclusters and particles. It also shows that there is an opposite driving force for single atom Pd_1 regeneration at high temperature (923 K) and CO lean and O_2 rich conditions. In this ambient, which is very close to the initial synthesis conditions, PdO_x SNCs breaks apart, leaving doped Pd_1 at terraces as well as surface-residing Pd_{ad} atoms that quickly migrate to more favorable step sites where it forms a more stable Pd_1O_4 state.

Supplementary Note 5

CO abatement during RT-CO activation

As confirmed by both experimental results (Fig. 2c) and the DFT calculations (Supplementary Fig. 28), oxygen atoms that are 2-3 (i.e., 2.3) times of the loaded Pd atoms in the single-atom Pd_1/CeO_2 catalyst can be removed during the RT-CO activation process, being removed by CO via chemical reaction and forming CO_2. Therefore, the RT-CO activation which stimulates the cold start of engines can not only greatly enhance the CH_4 oxidation performance via transforming Pd_1 single atoms into PdO_x sub-nanometer clusters (SNCs), but also can deliver the chemical abatement of CO, which is one typical pollutant during the vehicle cold-start when the temperature of catalytic converter is not effective (high enough) to drive the catalytic removal of CO.

With the CO/O to Pd ratio, it is possible to estimate the amount of CO that can be removed during the RT-CO activation process. Although the quantities vary by model, on average, for cars and light-duty trucks, only one standard catalytic converter contains about 3-7 grams of platinum, 2-7 grams of palladium, 1-2 grams rhodium. The amount of PGMs in the catalytic converter is higher for larger-engine SUVs and trucks and the average total can be up to 30 grams.

Here we assume that 5 grams of Pd is contained in one catalytic converter. Assuming 2-3 CO molecules per Pd atom can be converted into CO_2 by reacting with the interfacial O, 0.53-0.79 g of CO can be removed by transforming 1 g of Pd_1 single atoms. Therefore, 2.7-4 g CO can be removed for one vehicle during the first 1-2 min cold start of engine.

Supplementary Figures

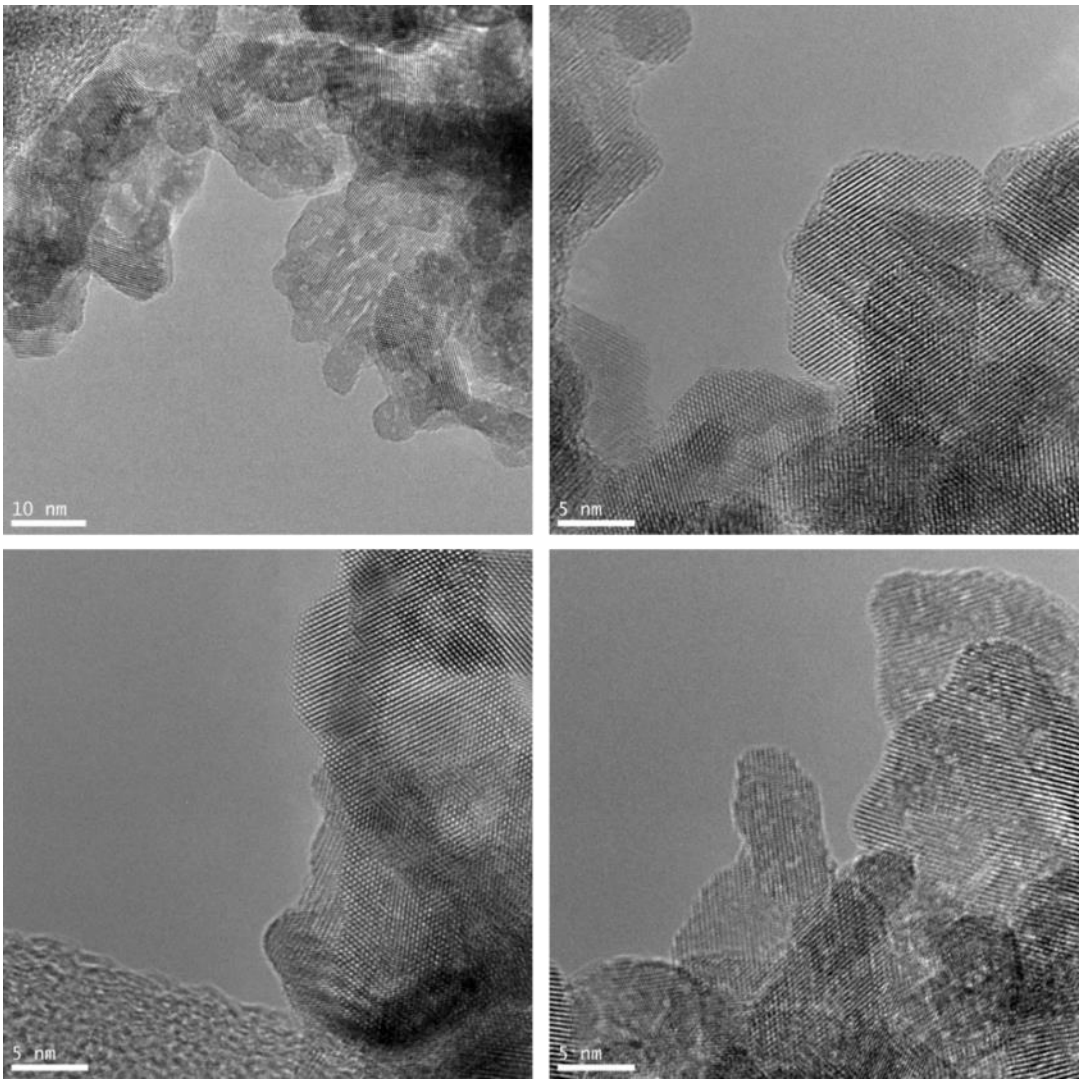

Supplementary Figure 1. High-resolution TEM (HR-TEM) images of the as-synthesized single-atom Pd_1/CeO_2 catalyst. All images present clean surface and clear (111) lattice spacing of polyhedral CeO_2 with no trace of Pd/PdO NPs or large clusters.

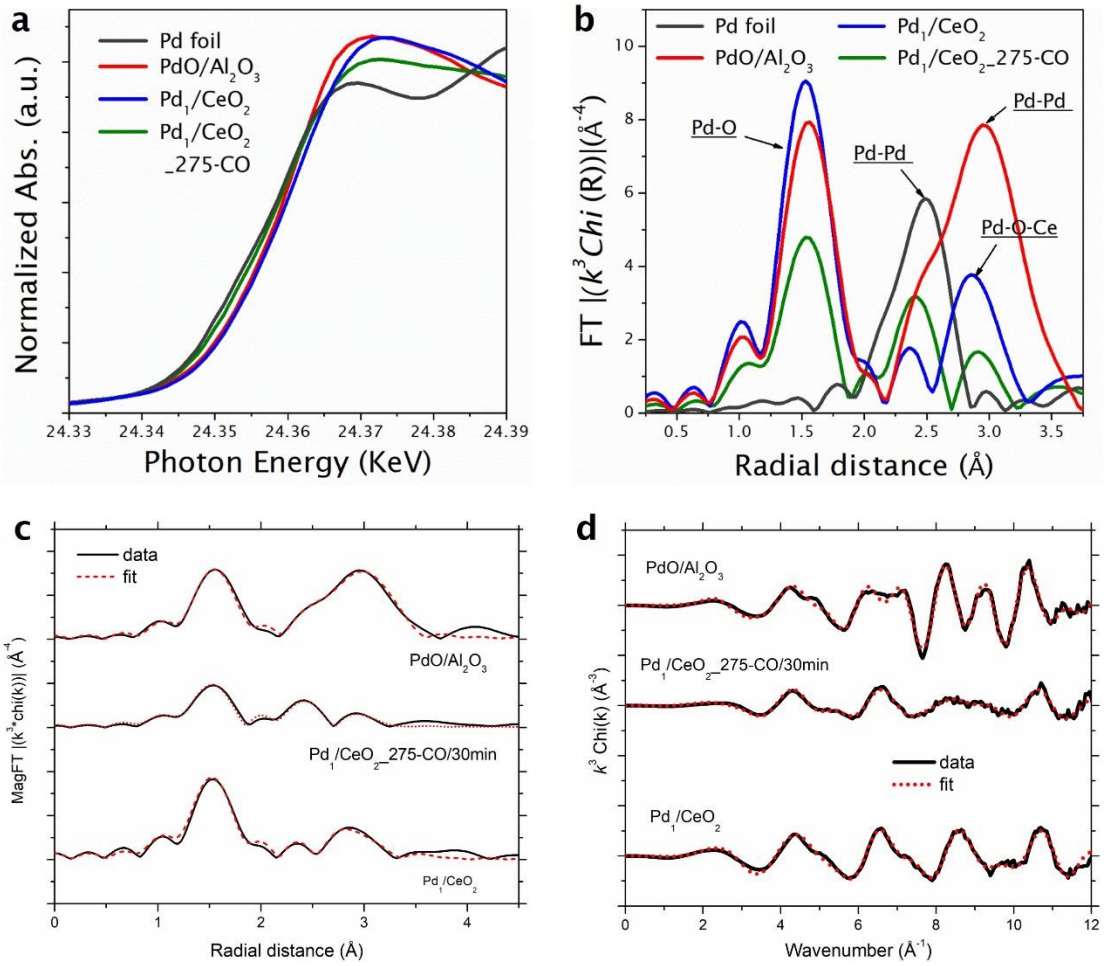

Supplementary Figure 2. (a) Pd K-edge XANES spectra of Pd foil, PdO/Al_2O_3, and Pd_1/CeO_2 in the as-synthesized state and after 275 ºC CO reduction. (b) Fourier transform of k^3-weighted EXAFS in R-space of Pd foil (x 0.2), PdO/Al_2O_3, and Pd_1/CeO_2 in the as-synthesized state and after 275 ºC CO reduction. (c) – (d) Best fitting results of the fourier-transformed k^3-weighted EXAFS in (b).

EXAFS of as-synthesized Pd_1/CeO_2 confirmed the dominance of Pd-O scattering signal as well as the absence of Pd-Pd scattering signal, conclusively indicating the atomic dispersion of Pd species (2b). XANES of as-synthesized Pd_1/CeO_2 at Pd K-edge indicate isolated Pd being in a cationic state (2a). As summarized in Supplementary Table 1, the fitting results suggest the Pd_1O_4 coordination of isolated Pd^{2+}, which can be assigned to a square-planar configuration preferred by Pd^{2+} as a d^8 ion (2c and 2d)[27].

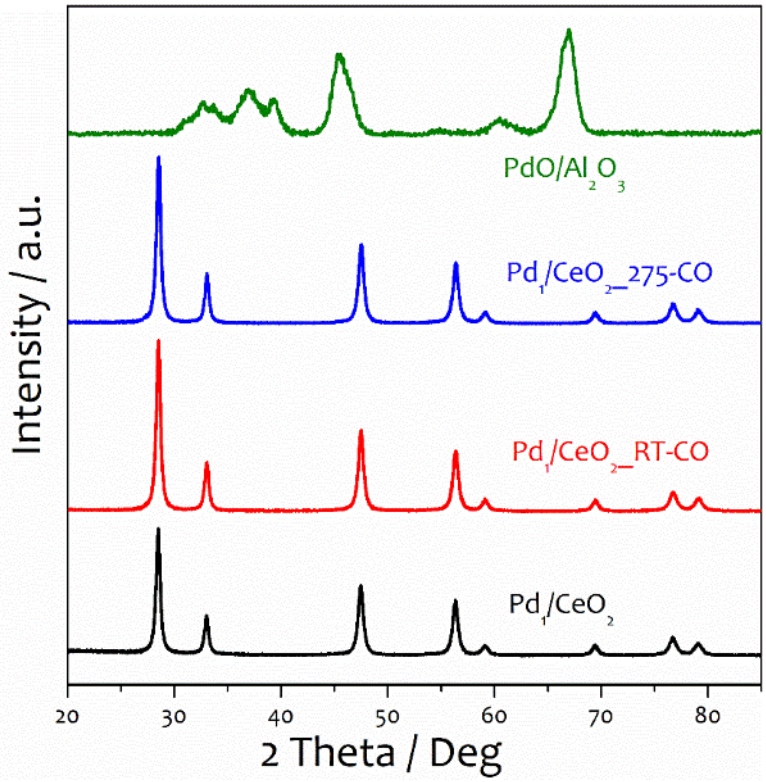

Supplementary Figure 3. Powder X-ray diffraction (XRD) patterns of Pd_1/CeO_2 and PdO/Al_2O_3 catalysts in the as-synthesized state and Pd_1/CeO_2 catalysts after RT-CO and 275-CO treatments.

For Pd/CeO_2 catalysts, all the diffraction peaks can be readily indexed to fluorite ceria (PDF # 34-0394), with no PdO/Pd detected, indicating high Pd dispersions and/or small particle sizes in as-synthesized PdO/Al_2O_3 and Pd_1/CeO_2 even after CO reduction at 275 ^oC.

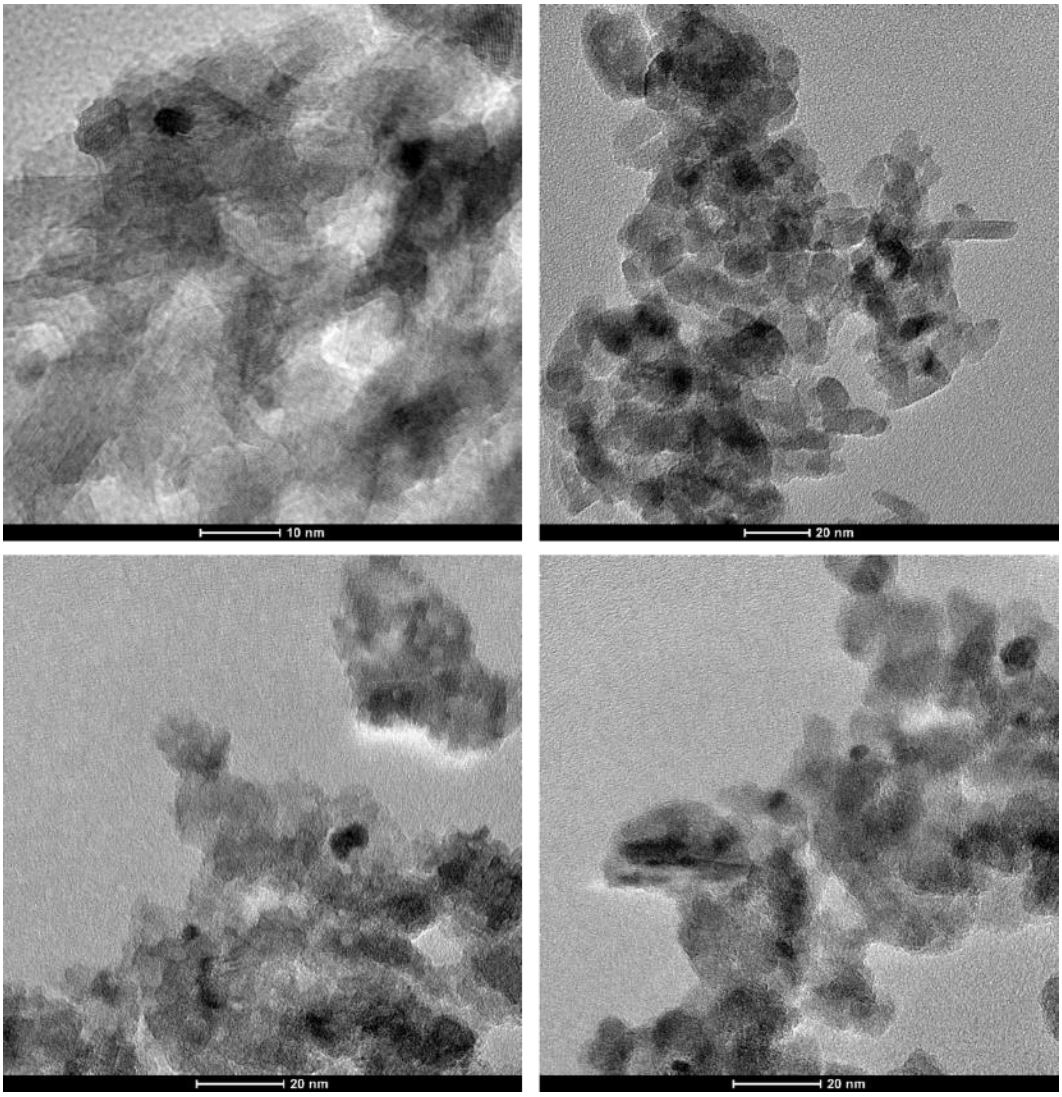

Supplementary Figure 4. TEM images of as-synthesized PdO/Al_2O_3 catalyst showing the presence of 2-5 nm PdO NPs in the as-synthesized catalyst.

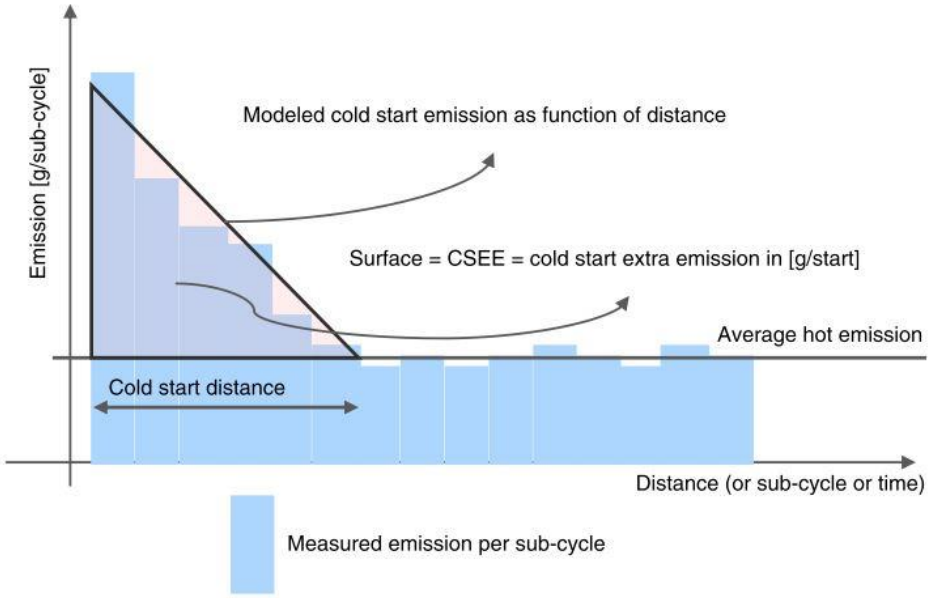

Supplementary Figure 5. A schematic diagram of the vehicle emissions during a cold-start test with a repetitive test cycle and a sketch of the empirical model. This figure is reproduced with permission from[28]. Typically, the emission levels are initially high (e.g., within 5 min), decreasing during the warm-up and stabilizing in the hot phase[29].

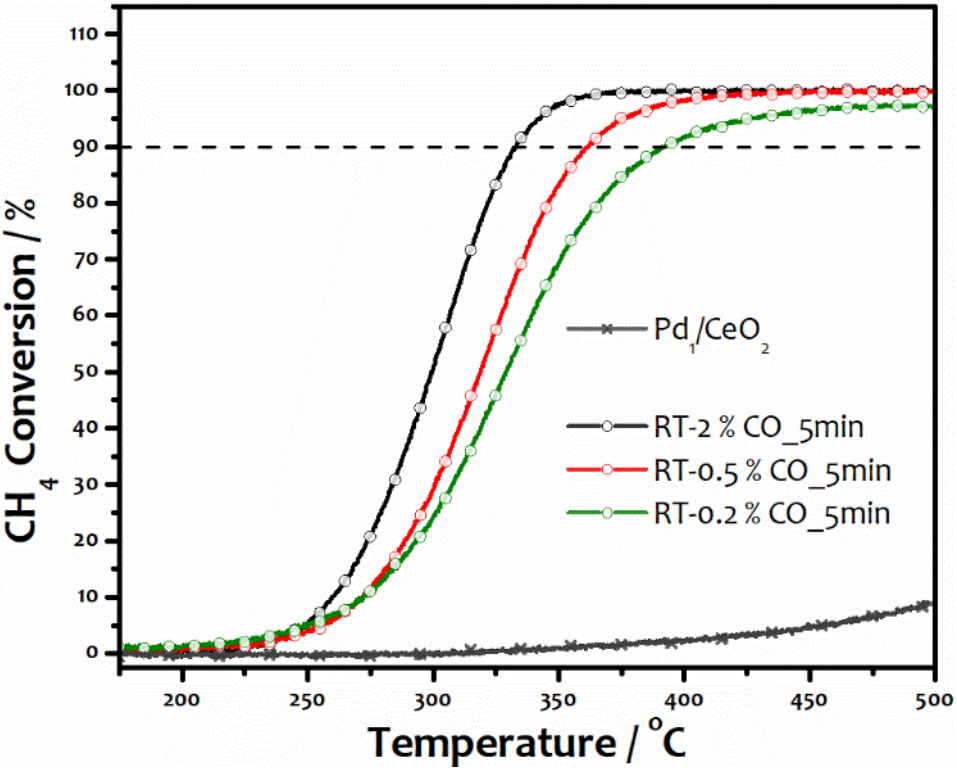

Supplementary Figure 6. Light-off measurements for CH_4 oxidation under dry conditions over Pd_1/CeO_2 in as-synthesized state and after RT-CO activation process in the presence of 14 % O_2 and CO with different concentration (0.2 % - 2 %). Reaction condition: 680 ppm CH_4, 5 % CO_2, 14 % O_2, N_2 balance. The total flow was kept the same for different RT-CO treatments.

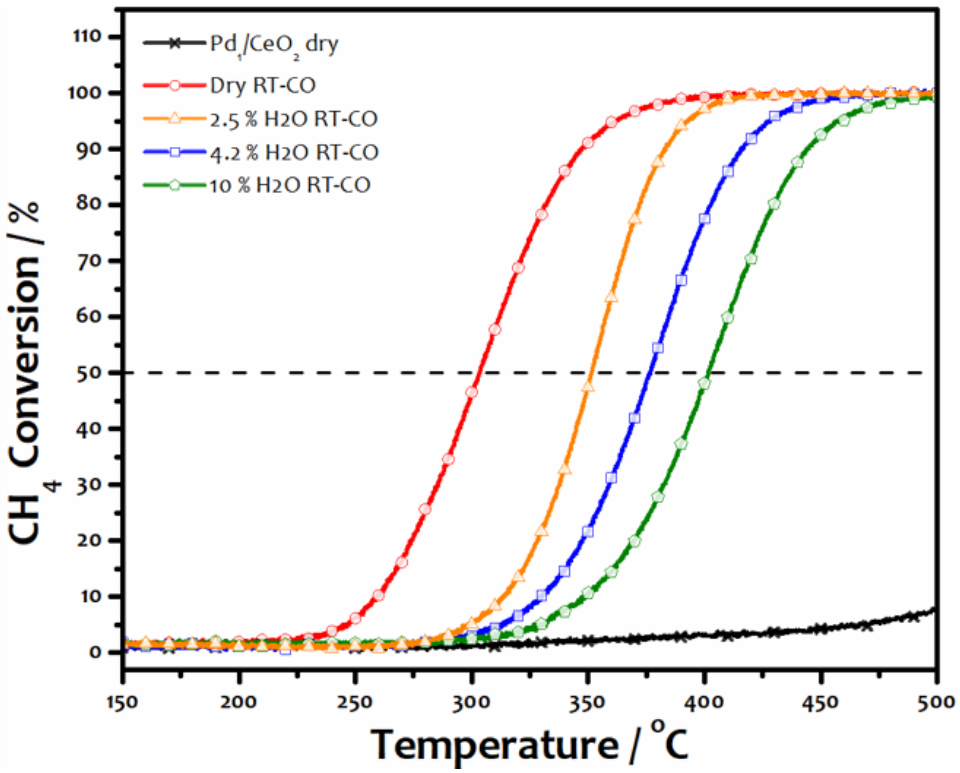

Supplementary Figure 7. CH_4 light-off performance in the presence of different amounts of H_2O over single-atom Pd_1/CeO_2 catalyst after RT-CO activation in the presence of 2 % CO and 14 % O_2. Reaction condition: 680 ppm CH_4, 5 % CO_2, 14 % O_2, N_2 balance. RT-CO: 2 % CO, 14 % O_2, N_2 balance. RT-CO lasts for 5 min unless otherwise specified.

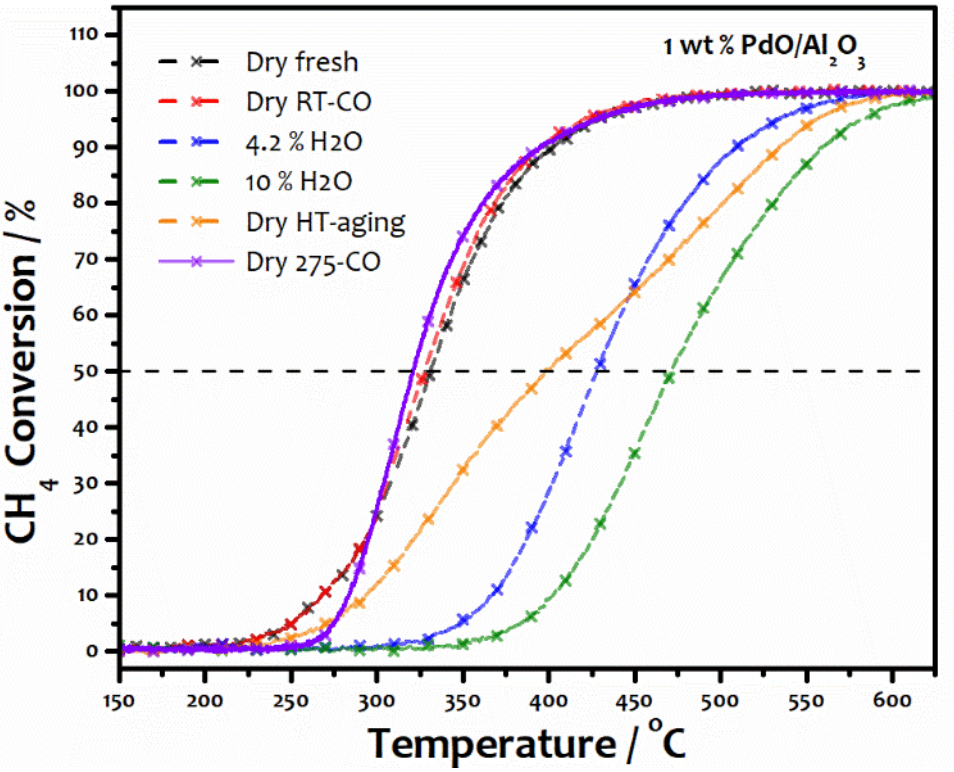

Supplementary Figure 8. CH_4 light-off performance of PdO/Al_2O_3 catalyst in as-synthesized state under dry and wet conditions with different amount of H_2O, as well as after RT-CO, hydrothermal aging (HTA), and 275-CO treatments. Reaction condition: 680 ppm CH_4, 5 % CO_2, 14 % O_2, N_2 balance. RT-CO: 2 % CO, 14 % O_2, N_2 balance. RT-CO lasts for 5 min unless otherwise specified. HTA: 10 % H_2O, and 14 % O_2 with N_2 balance, 275-CO: 2 % CO with N_2 balance.

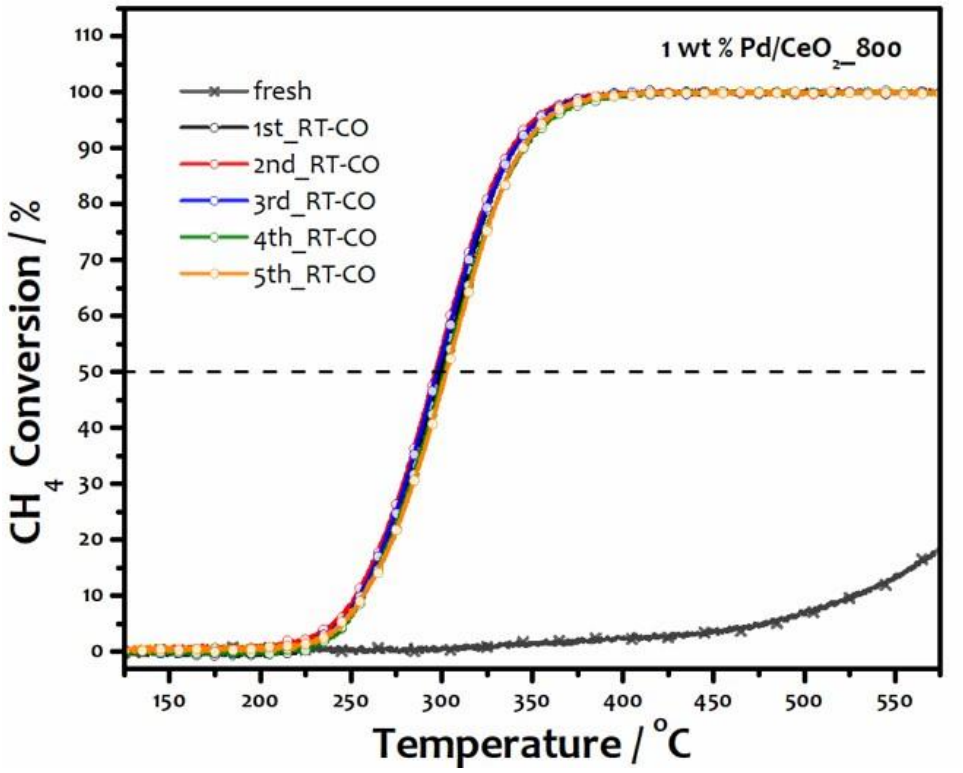

Supplementary Figure 9. CH_4 light-off performance under dry condition of Pd_1/CeO_2 in as-synthesized state and after 5 consecutive RT-CO activation and light-off cycles. Before each light-off measurement, RT-CO for 5 min was conducted to mimic cold starts of engine. Reaction condition: 680 ppm CH_4, 5 % CO_2, 14 % O_2, N_2 balance. RT-CO: 2 % CO, 14 % O_2, N_2 balance. RT-CO lasts for 5 min unless otherwise specified.

As shown, after 5 cycles, the RT-CO activated low-temperature activity was almost completely preserved, confirming the excellent cycling stability of single-atom Pd_1/CeO_2 system.

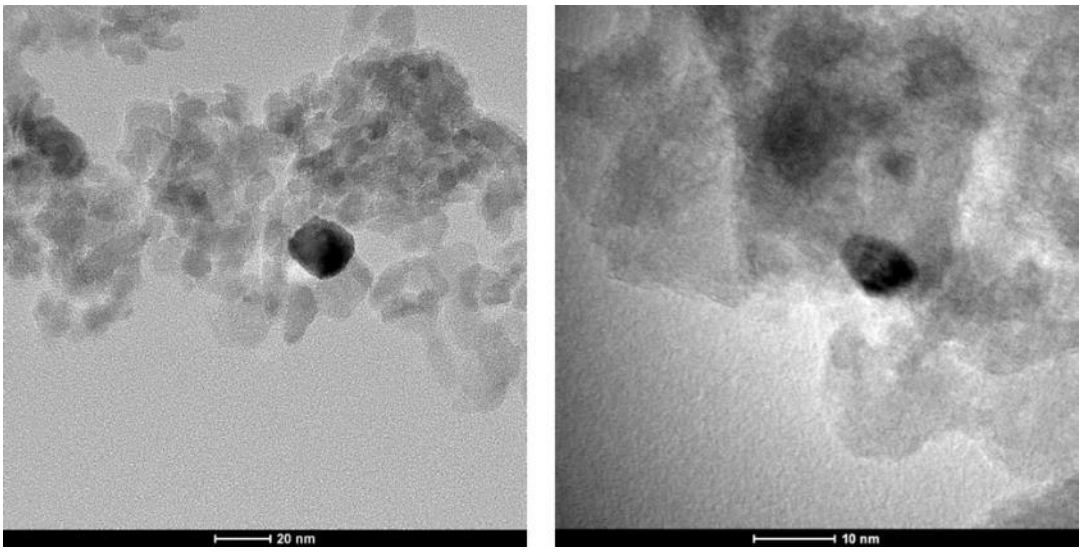

Supplementary Figure 10. TEM images of PdO/Al_2O_3 catalyst after hydrothermal aging at 750 ^oC, showing the presence of > 10-20 nm PdO NPs due to the growth (sintering) of small NPs (2-5 nm).

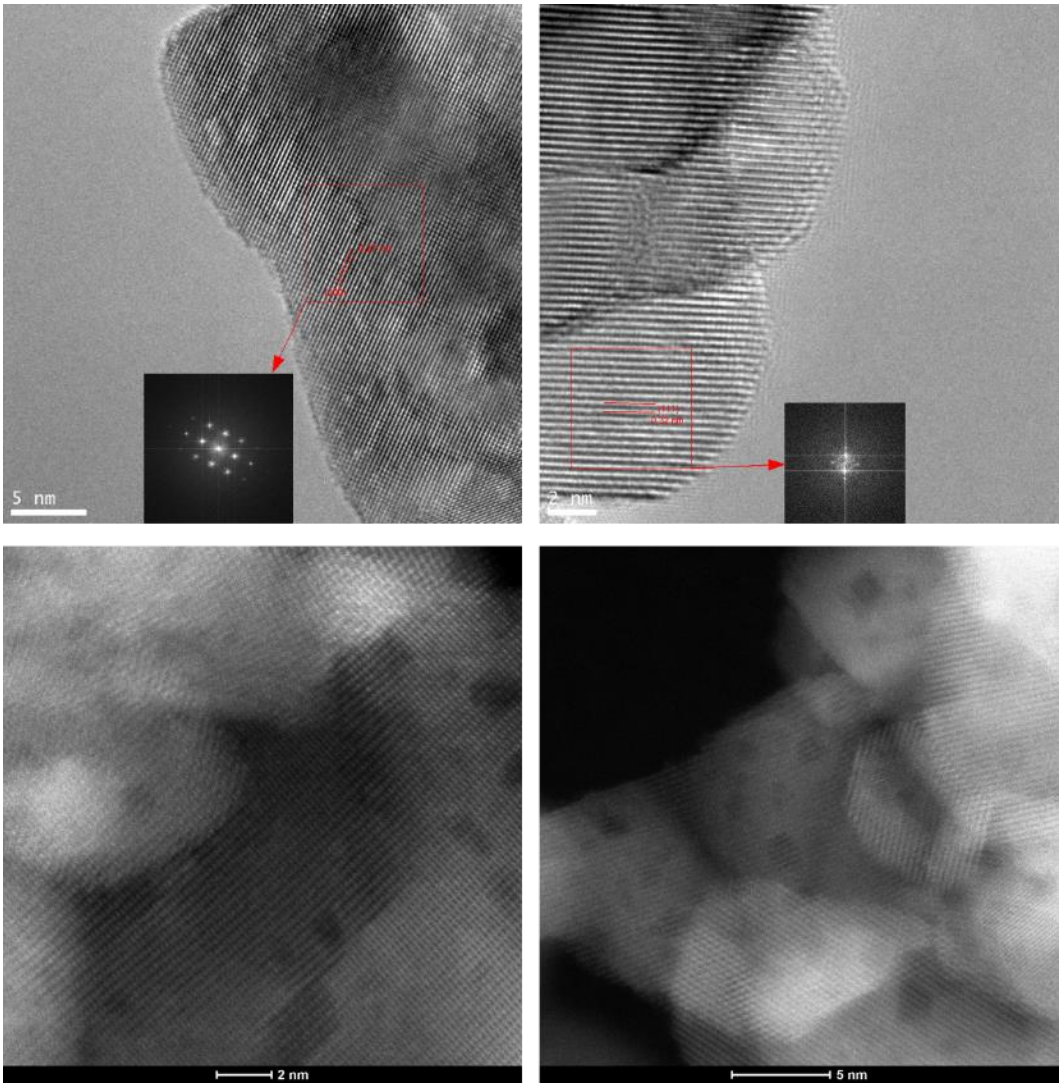

Supplementary Figure 11. HR-TEM and AC-STEM images of Pd_1/CeO_2 after RT-CO activation for 5 min at room temperature. Based on careful TEM investigations, there was no clear evidence of NPs formation after RT-CO activation.

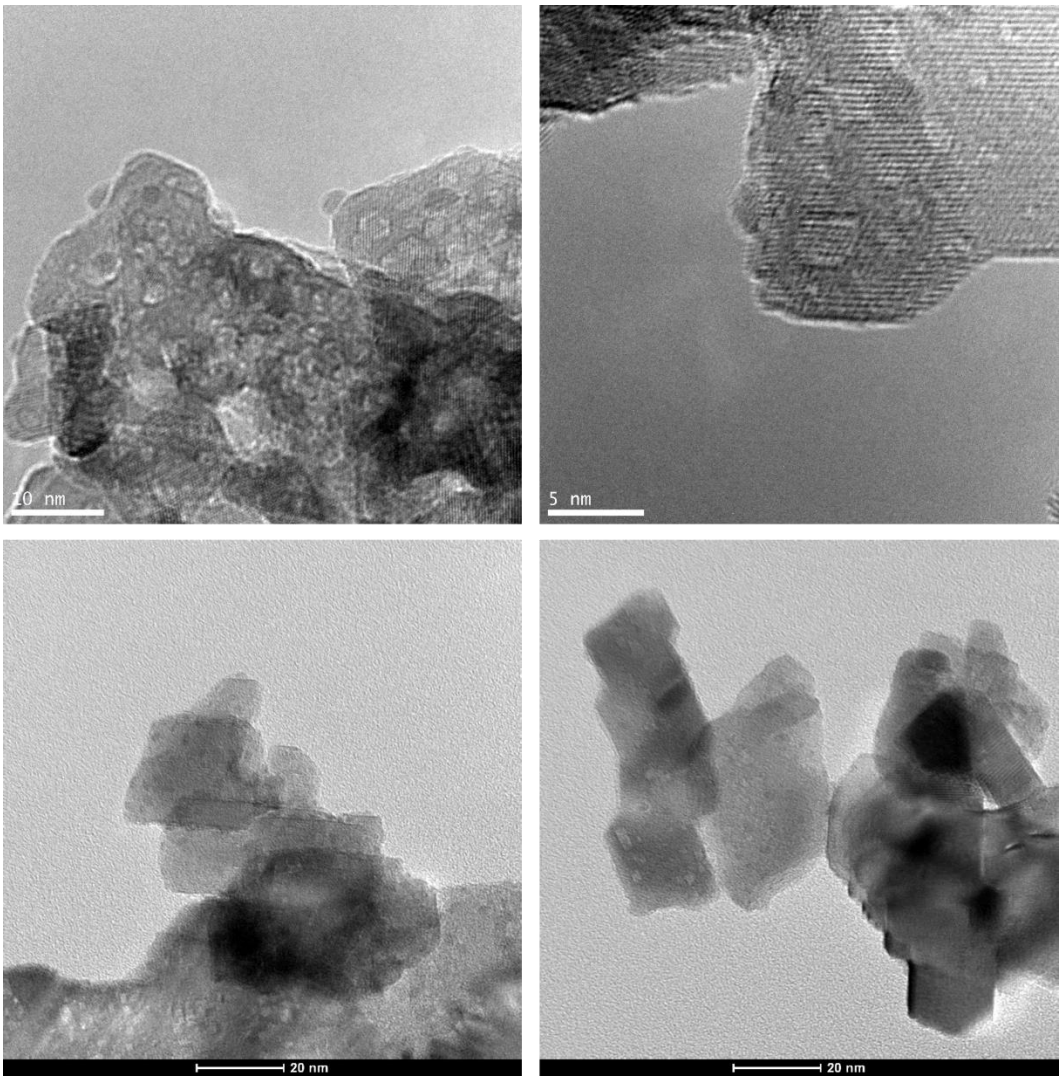

Supplementary Figure 12. HR-TEM images of single-atom Pd_1/CeO_2 after being reduced by 2 % CO at 275 ^oC for 30 min (275-CO). Formation of 2-3 nm Pd/PdO NPs upon 275-CO reduction was clearly observed.

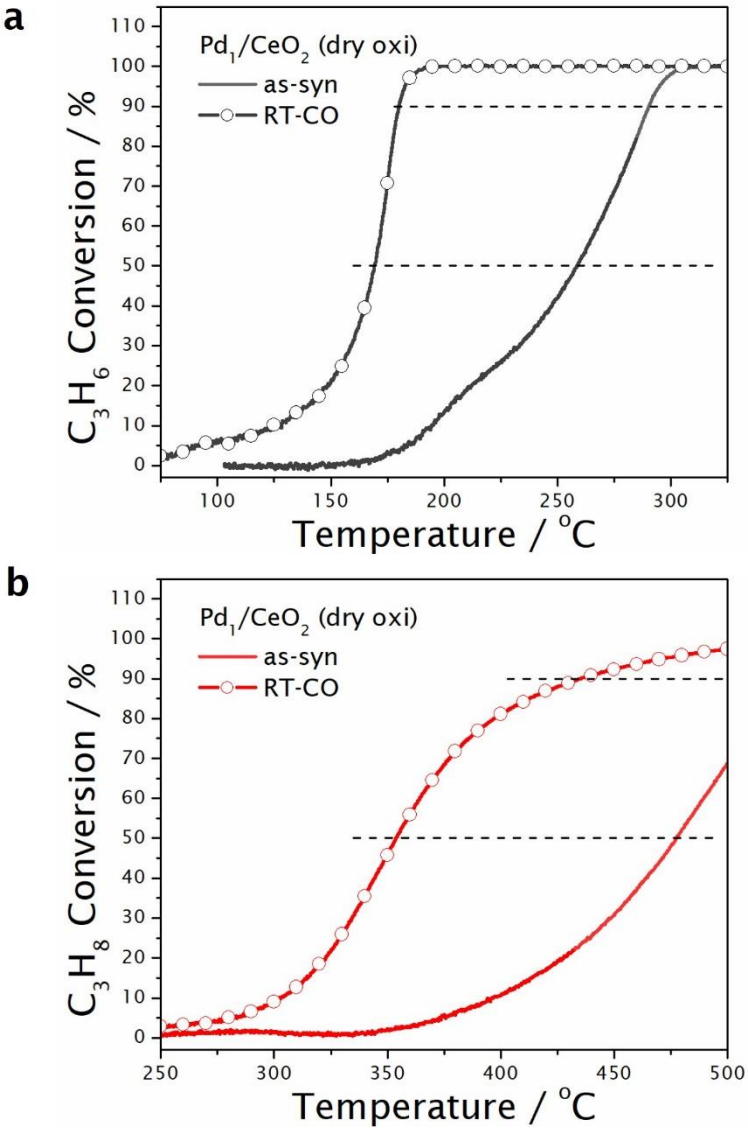

Supplementary Figure 13. Dry hydrocarbons (HCs) light-off performance of Pd_1/CeO_2 catalyst in as-synthesized state and after RT-CO treatment. Reaction conditions: 700 ppm C_3H_8, 700 ppm C_3H_6, 7 % O_2, balanced with N_2, GHSV of 200 L/g-h**.**

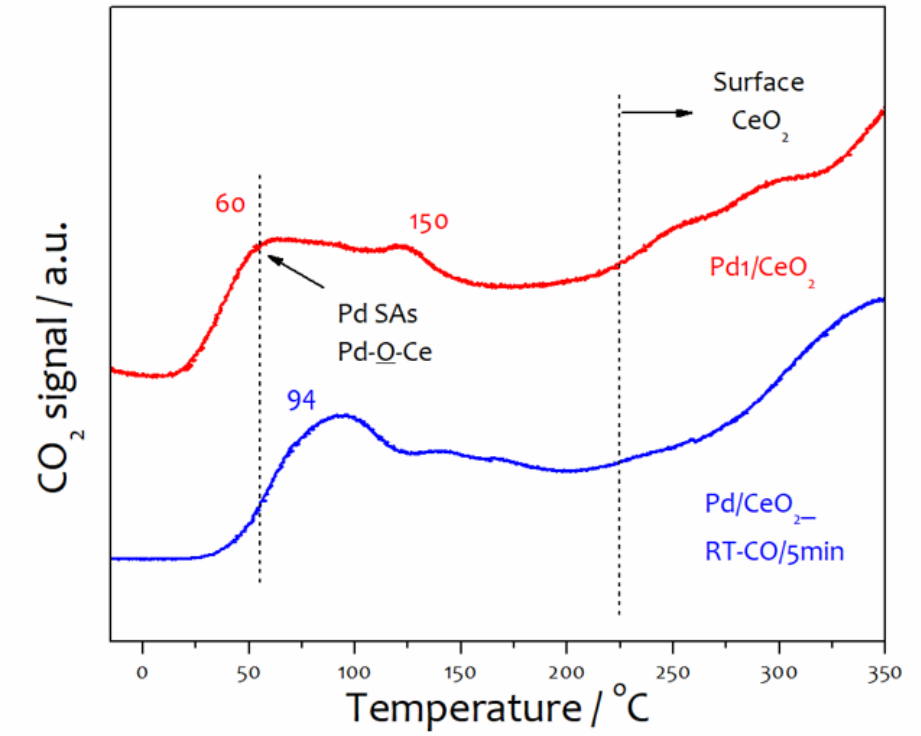

Supplementary Figure 14. Temperature-programmed reduction profiles by CO (CO-TPR) of the as-synthesized Pd_1/CeO_2 and Pd_1/CeO_2 after RT-CO treatment for 5min.

The low-temperature reduction with onset temperature of ~ 25 ºC has been attributed to the reduction of isolated Pd^{2+} on CeO_2 surface[27]. Notably, the low-temperature reducibility was greatly decreased after the RT-CO treatment, suggesting that isolated Pd^{2+} were transformed into other species.

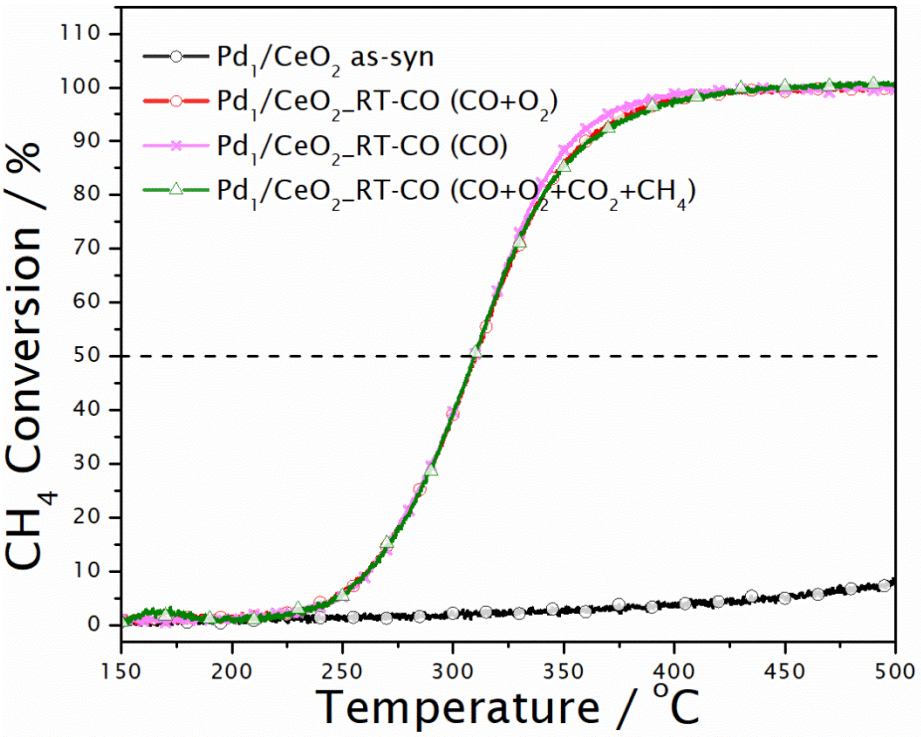

Supplementary Figure 15. Light-off performance for dry CH_4 oxidation of Pd_1/CeO_2 in as-synthesized state and after RT-CO (2 % CO) activation process in the presence and absence of O_2 (14 %), CO_2 (5 %), and CH_4 (680 ppm). Reaction condition for dry CH_4 oxidation: 680 ppm CH_4, 5 % CO_2, 14 % O_2, N_2 balance, 300 L g^{-1} h^{-1}.

The above light-off curves were collected using the same catalyst (bed). Before each activation treatment, the catalyst was heated in dry reaction stream up to 800 °C. As shown, excess amount of O_2 and other components in CH_4 oxidation reaction stream didn't influence the effectiveness of the RT-CO activation.

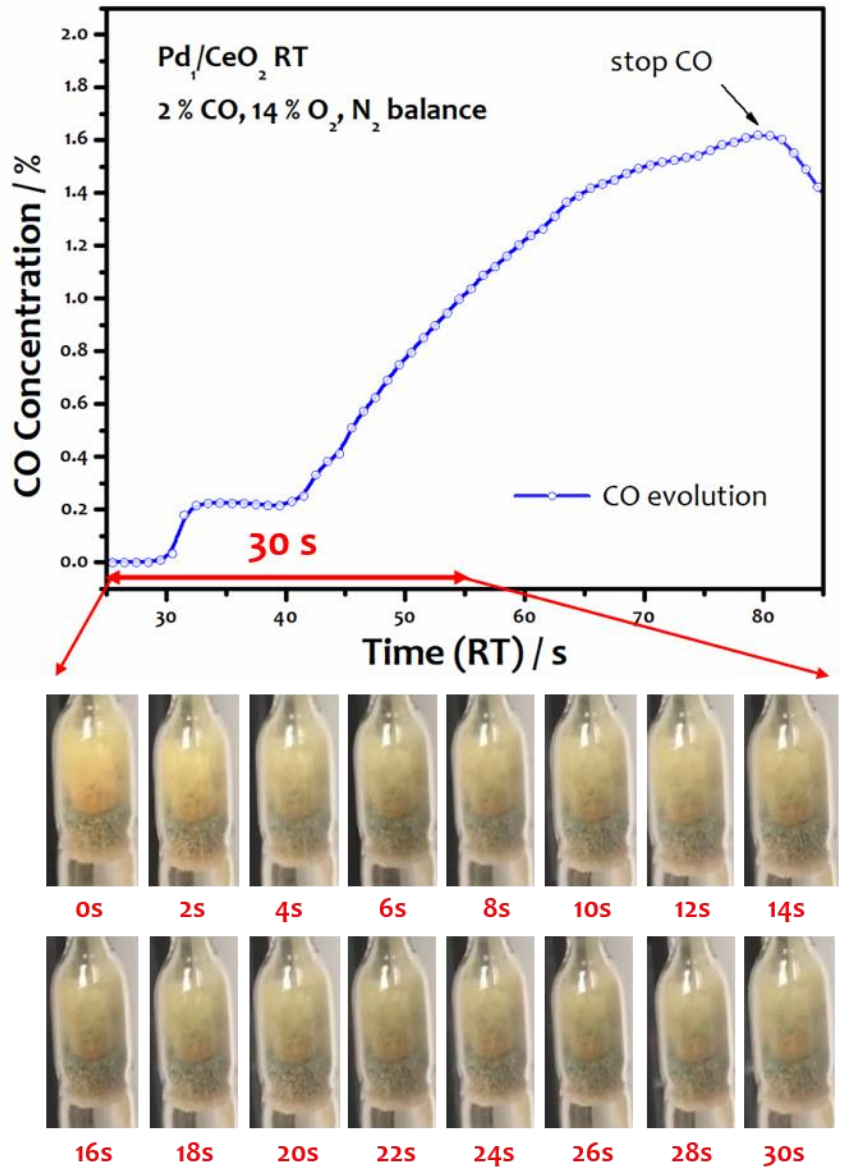

Supplementary Figure 16. CO evolution profile during the RT-CO (25 ^{o}C) processes. Conditions: 2 % CO, and 14 % O_2 with N_2 balance, 150 sccm total flow. Effluent from the catalyst bed was analyzed by an on-line continuous FTIR with 1 Hz acquisition frequency.

Digital pictures showed the color change of the catalyst bed within the initial 30 s. To clearly observe the color change during RT-CO, Pd_1/CeO_2 catalyst powders were diluted by SiC with a wight ration of 1:10, rather than 1:25 for light-off measurements.

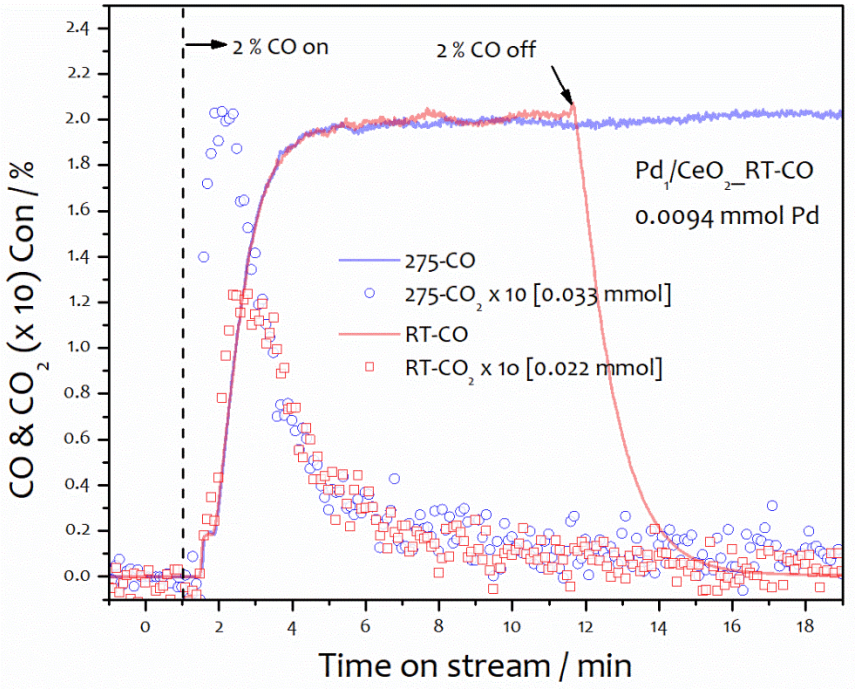

Supplementary Figure 17. CO_2 and CO evolution profiles during CO reduction at 275 °C (275-CO). Conditions: 2 % CO, N_2 balance, 130 ml/min. Before performing CO reduction at 275 °C, as-synthesized single-atom Pd_1/CeO_2 catalyst was pre-treated in N_2 at 350 °C to clean the surface.

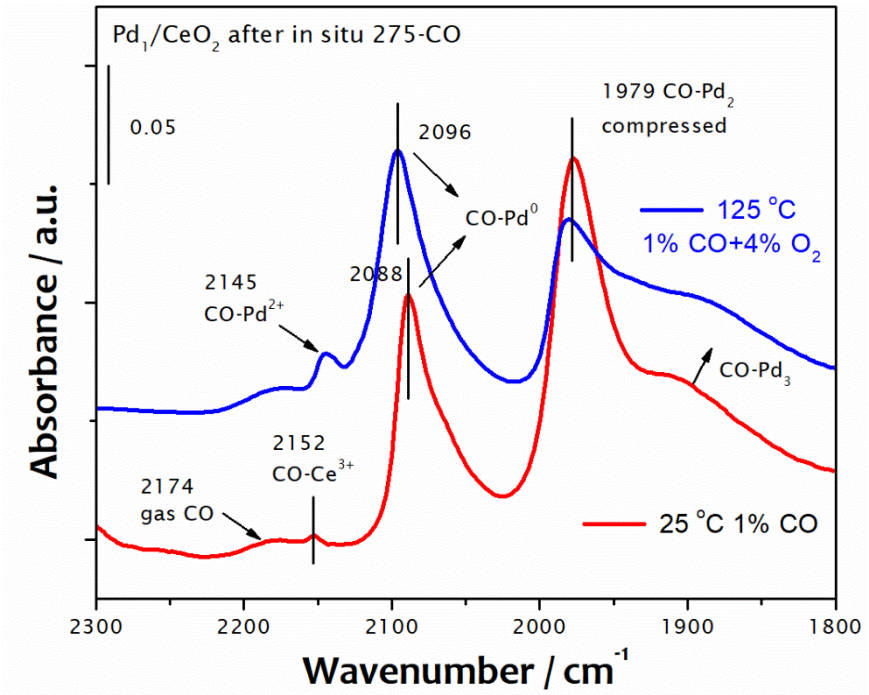

Supplementary Figure 18. DRIFTS of single-atom Pd_1/CeO_2 catalyst after *in situ* CO reduction at 275 °C for 30 min. After 275-CO, catalyst was purged with helium at 275 °C before cooling down to room temperature. Then DRIFTS was conducted at 25 °C in flowing 1 % CO/He to clarify surface Pd species.

As shown (red line), only Pd NPs mostly in a metallic state can be probed by CO adsorption. It should be noted, after long time exposure to air or an oxidative atmosphere, metallic Pd NPs will gradually turn into a mixed Pd/PdO phase since PdO is the thermodynamically stable phase for palladium at low temperatures in air[30]. As shown (blue), at 125 °C in a CO/O_2 mixture, Pd^{2+} cations are probed by CO.

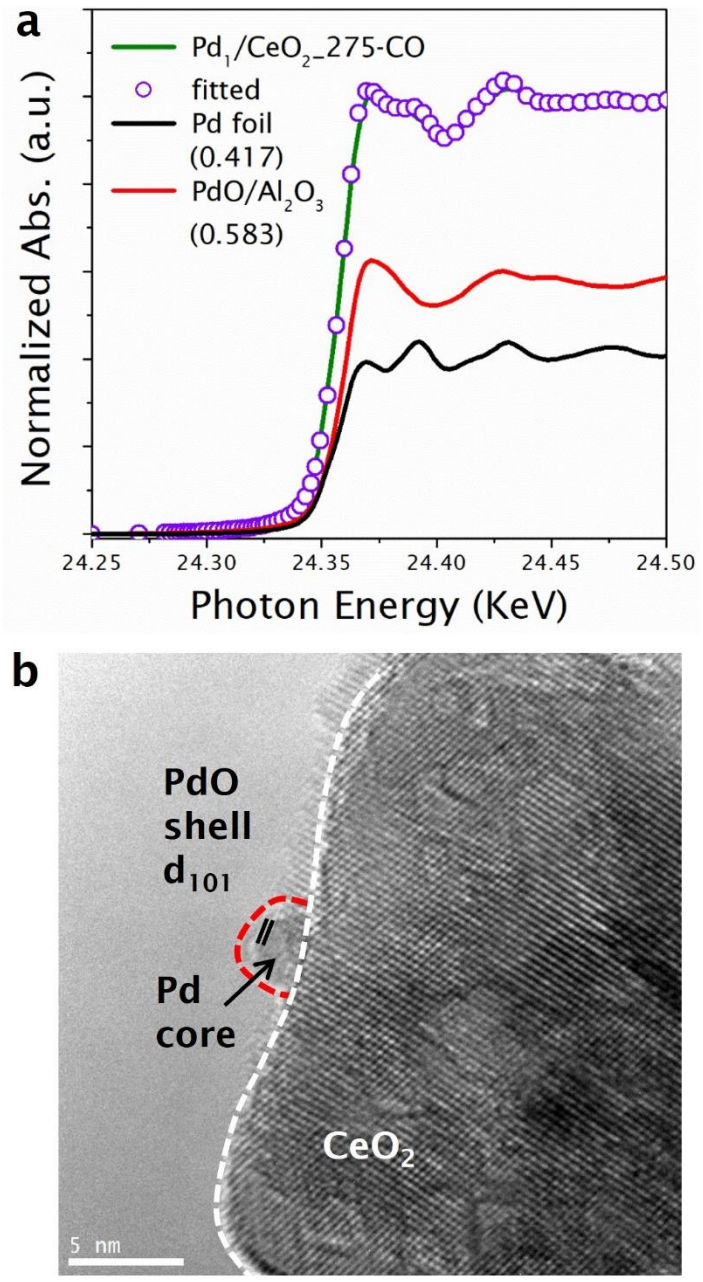

Supplementary Figure 19. (a) Linear combination fitting of XANES spectrum of Pd_1/CeO_2_275-CO. (b) HR-TEM image of the 275-CO reduced Pd_1/CeO_2. The XANES spectrum of 275-CO reduced Pd_1/CeO_2 can be fitted by a linear combination of Pd and PdO phases, clearly indicating the coexistence of Pd and PdO.

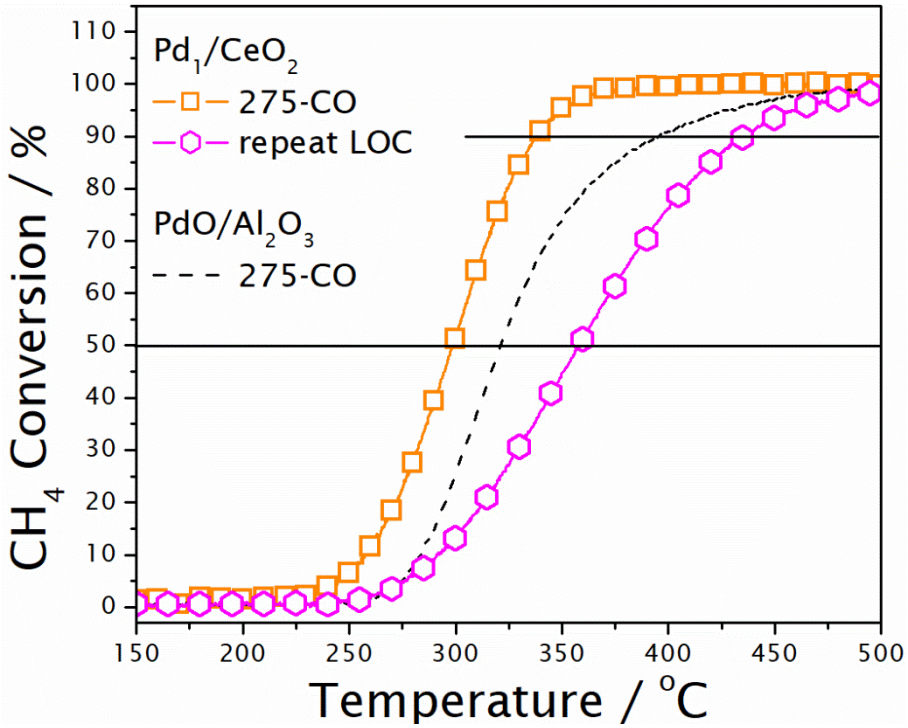

Supplementary Figure 20. CH_4 light-off performance under dry condition of Pd_1/CeO_2 catalyst after CO reduction at 275 °C for 30 min (275-CO).

Two successive light-off measurements were conducted showing the performance degradation of the pre-reduced Pd_1/CeO_2 catalyst. PdO/Al_2O_3 after an identical 275-CO treatment was also presented for reference.

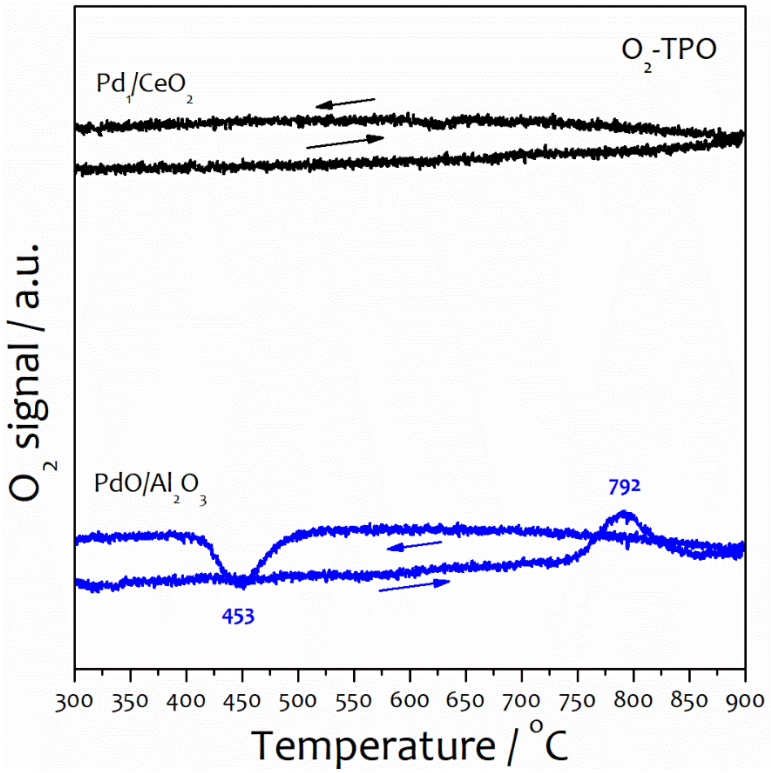

Supplementary Figure 21. Temperature-programmed oxidation in O_2 (O_2-TPO) over the Pd_1/CeO_2 and PdO/Al_2O_3 catalysts in the as-synthesized state.

For PdO NPs supported on Al_2O_3, O_2 release during the heating above 750 °C and O_2 uptake during the following cooling at much lower temperatures (453 °C) were observed. The high-temperature decomposition of PdO into metallic Pd in oxidative atmosphere has been well reported and is responsible for the performance decrease of Pd catalysts during CH_4 oxidation. Furthermore, upon repeated reduction (decomposition) and re-oxidation, particles (Pd/PdO) sintering cannot be avoided. In contrast, the single-atom Pd_1/CeO_2 catalyst showed nearly silent signal during O_2-TPO, clearly suggesting that the strong Pd-O interactions were not destroyed up to 900 °C. This undoubtedly confirms the superior structural stability of the single-atom Pd_1/CeO_2 system under harsh conditions, which is also consistent with the atom-trapping (AT) observation that formation of strong metal-ceria interactions enables the stabilization of isolated metal cations (e.g., Pt, Pd, Cu, etc.) on CeO_2 surface, forming a series of SACs via an oxidative dispersion mechanism[3,27,31-33].

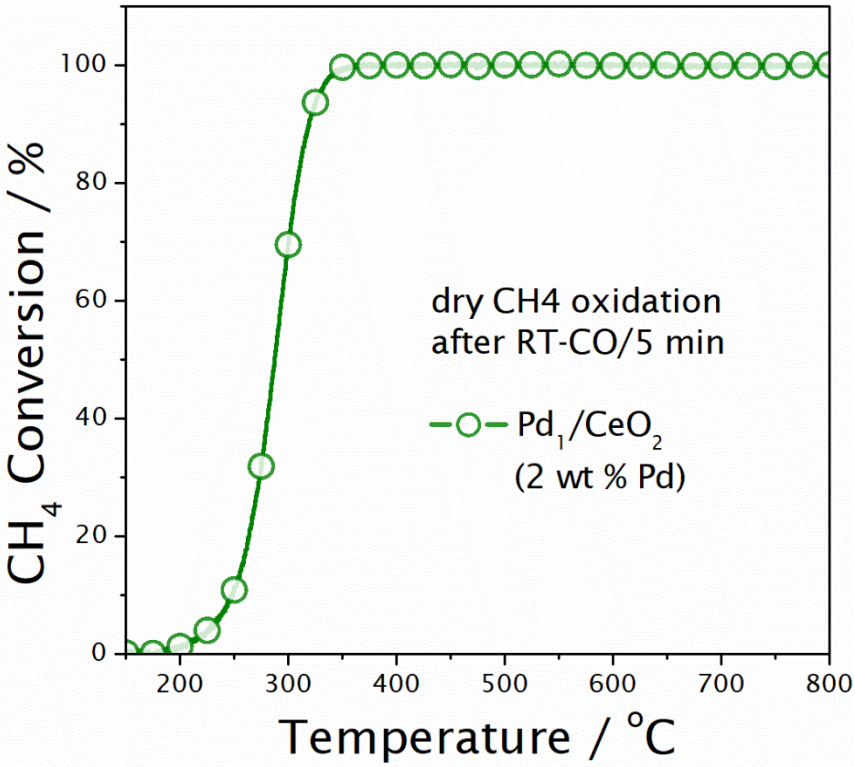

Supplementary Figure 22. Dry CH_4 oxidation over a single-atom Pd_1/CeO_2 (2 wt. %) catalyst after RT-CO treatment for 5 min. Reaction conditions: 680 ppm CH_4, 5 % CO_2, 14 % O_2, N_2 balance, GHSV = 300,000 ml g^{-1} h^{-1}.

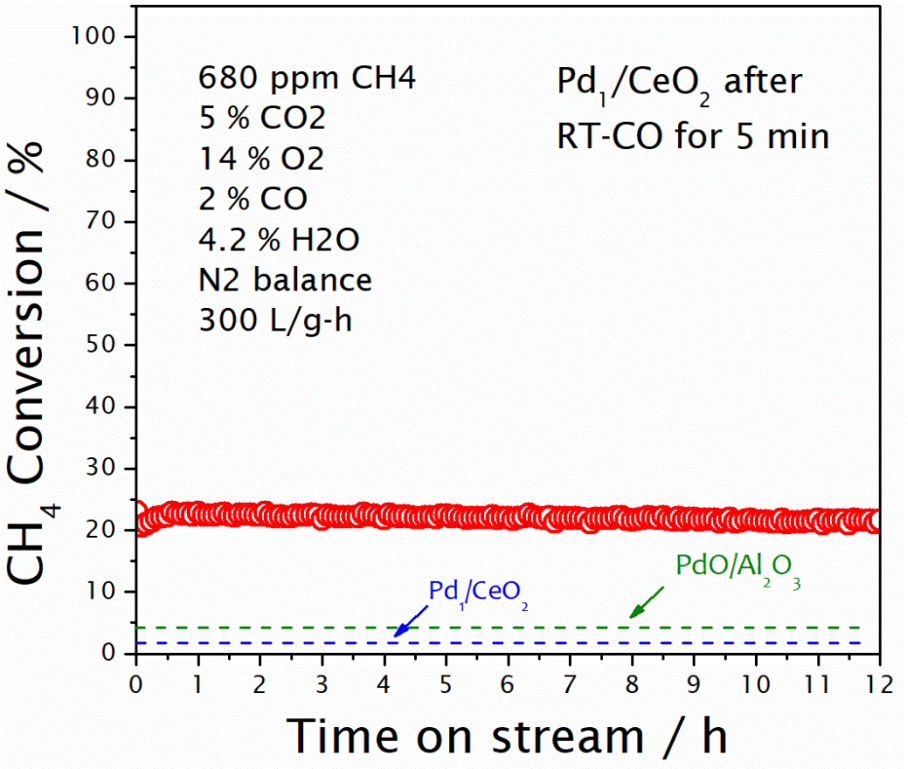

Supplementary Figure 23. Time-on-stream catalytic CH_4 oxidation in the presence of CO_2, CO, and H_2O at 350 ^oC over the RT-CO (5 min) activated Pd_1/CeO_2 catalyst. Reaction conditions are indicated in the figure.

CO, CO_2, and H_2O are all included to be closer to the real engine exhaust of NGVs. The non-activated catalyst (Pd_1/CeO_2) as well as PdO/Al_2O_3 showed extremely low activity (< 5 % CH_4 conversion) under identical conditions.

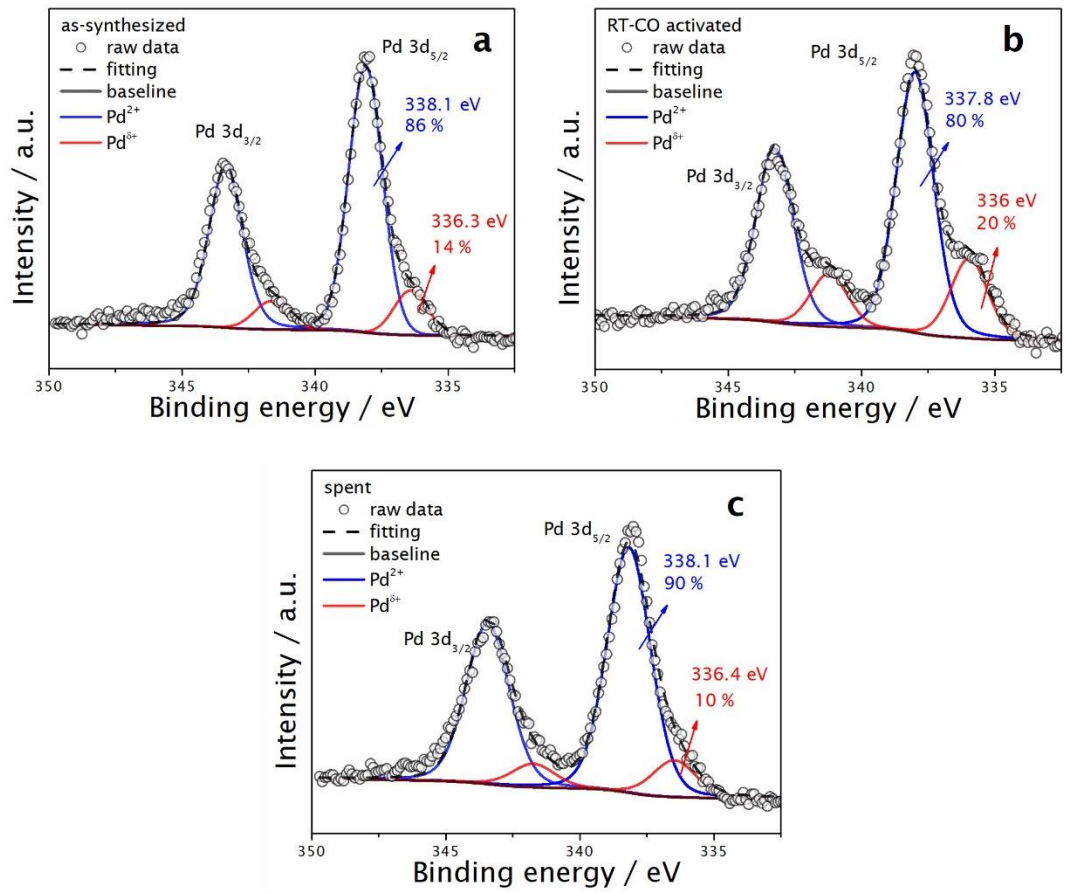

Supplementary Figure 24. X-ray photoelectron spectroscopy (XPS) results in the Pd 3d region of as-synthesized Pd_1/CeO_2 catalyst (a), the RT-CO/5 min activated catalyst (b), and the spent catalyst after dry CH_4 oxidation up to 800 ^oC (c).

As shown, as-synthesized Pd_1/CeO_2 catalyst is dominated by Pd^{2+} (86 %). After RT-CO activation for 5 min, the partially reduced $Pd^{\delta+}$ increased to 20 %, suggesting the slight reduction of surface Pd species which is consistent with the XANES results (Fig. 3c). The percentage of $Pd^{\delta+}$ species in the activated catalyst could be higher considering possible surface reoxidation after the activation, when CO is stopped and the activated sample is exposed to air before being transferred to the XPS chamber. After high-temperature CH_4 oxidation up to 800 ^oC, the spent catalyst exhibited a reduced population of $Pd^{\delta+}$ (10 %), very close to that in the fresh catalyst (14 %). This also agrees with the XANES results which indicate the regeneration of single-atom Pd_1/CeO_2 (Fig. 3c). Peak assignment of different Pd species is based on previous reports on Pd/CeO_2 system where metal strongly interacts with the support[34,35].

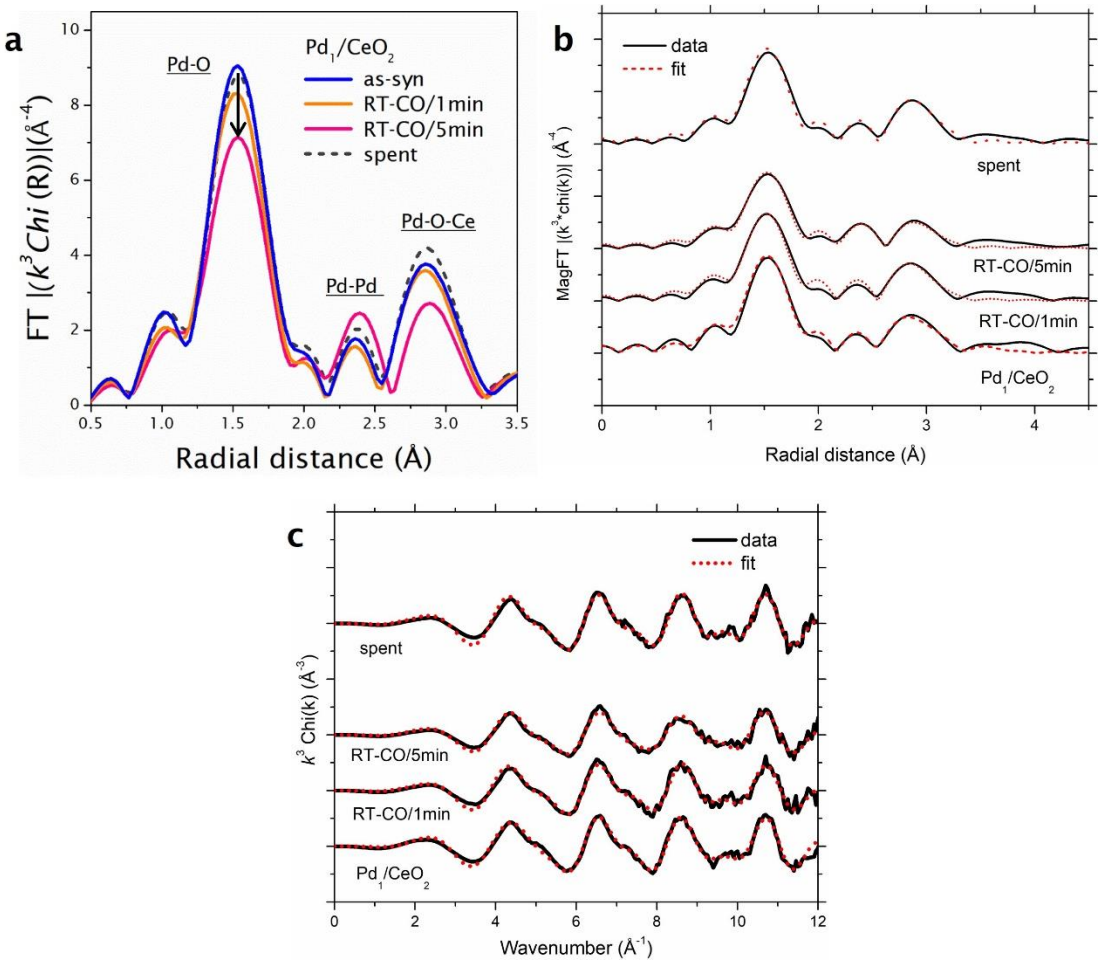

Supplementary Figure 25. (a) EXAFS spectra of Pd_1/CeO_2 in as-synthesized state, after RT-CO treatments for 1-5 min, and the spent Pd_1/CeO_2_RT-CO after CH_4 oxidation up to 800 ^oC. (b) – (c) Best fitting results of the fourier-transformed k^3-weighted EXAFS in (a).

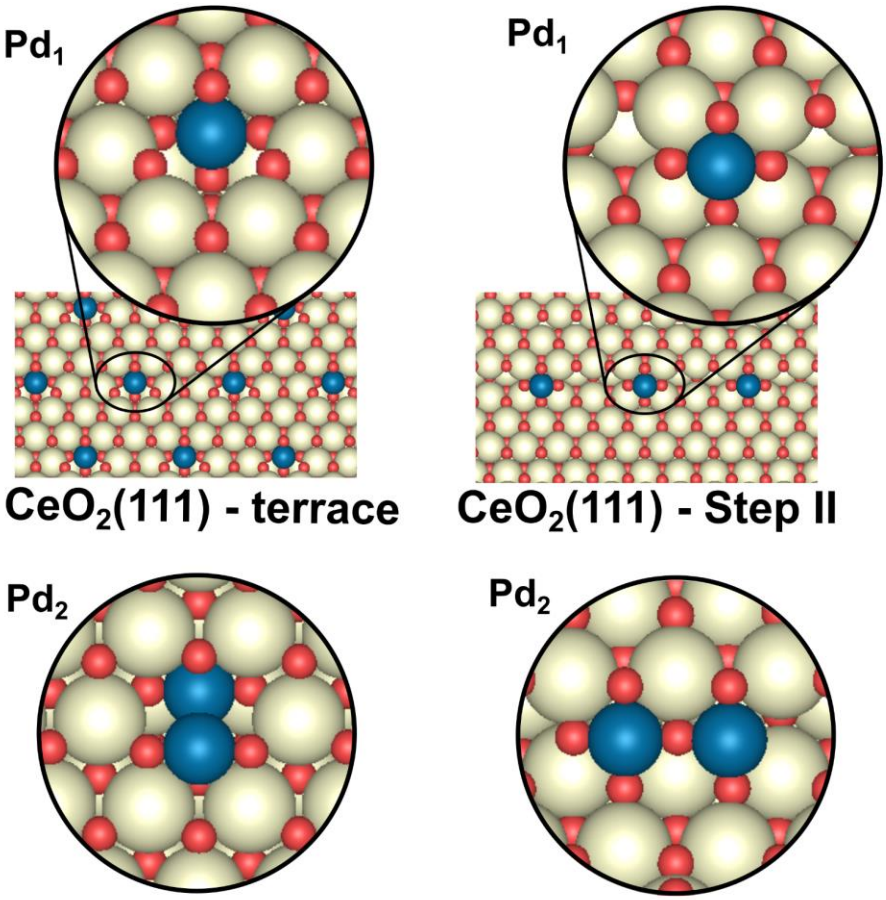

Supplementary Figure 26. DFT simulated low energy structures at 800˚C and 0.2 bar O_2(g) for Pd_1 and Pd_2 on the CeO_2(111) terrace and step surface models.

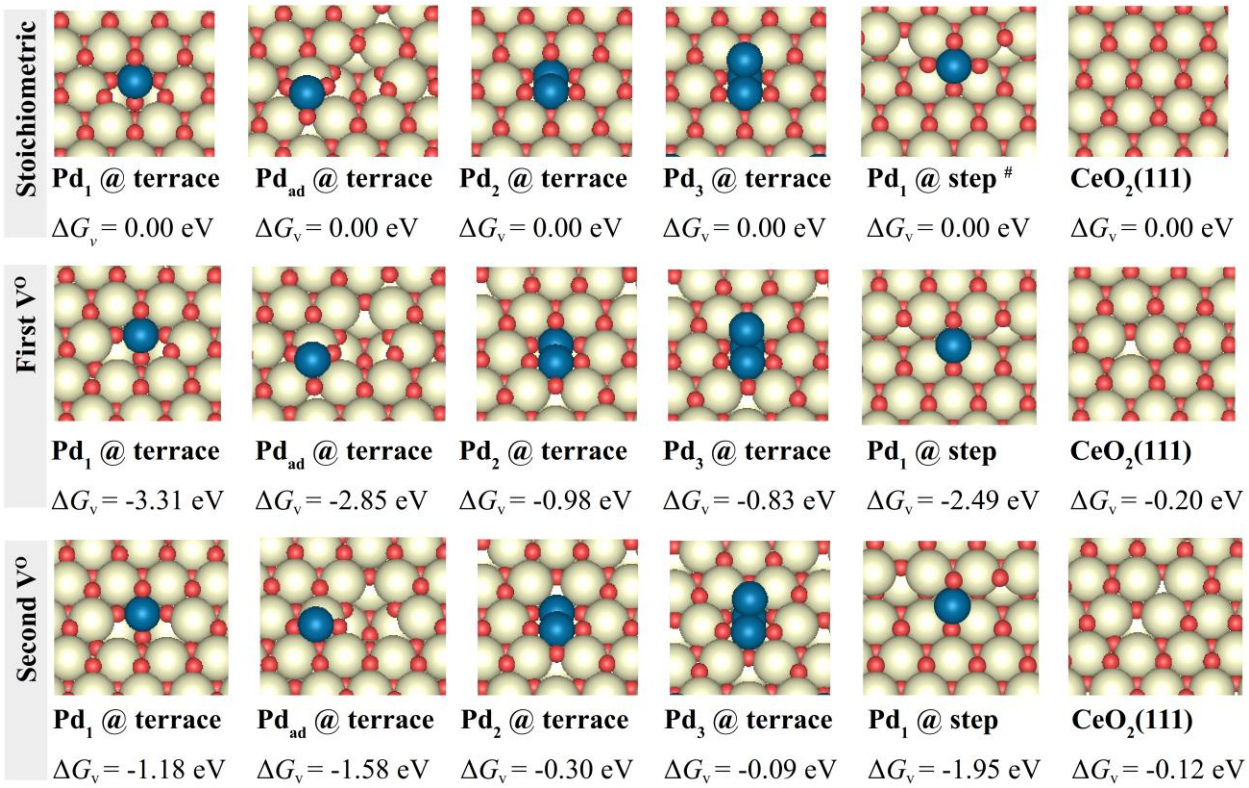

Supplementary Figure 27. DFT optimized structures and oxygen vacancy (V_O) formation free energetics, ΔG_v, of different Pd states at 25˚C and 0.02 bar of CO(g). The # symbol at "stoichiometric" Pd_1@step site indicates Pd_1O_4 stoichiometry but a substrate surface with 0.33 ML V_O (edge site) at the step, i.e., the thermodynamic favored state at synthesis conditions; the first and second V_O for the step model are relative the thermodynamically favored state.

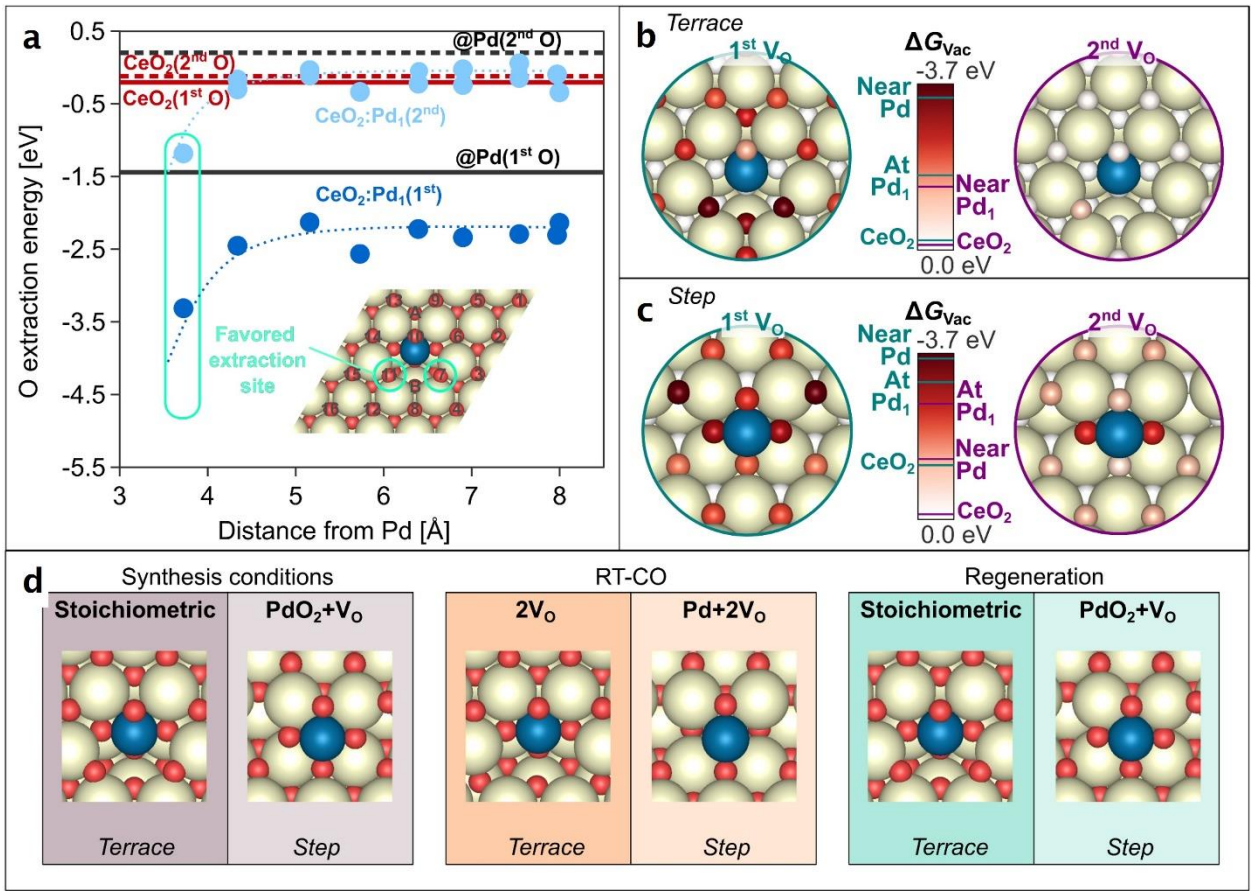

Supplementary Figure 28. (a) DFT computed oxygen vacancy (V_O) formation energies (via $O_{lattice}$ + CO(g) → CO_2(g)) 25˚C and 0.02 bar of CO(g) versus distance to the Pd_1 single-atom site for the extraction of the first (blue) and second (light blue) O atom per Pd atom (i.e., per nm^2). A (4×4) surface cell was used to evaluate the energetics. For comparison, the energy for extraction of oxygen at Pd_1 (oxygen directly connected to Pd_1, black) as well as from the pristine CeO_2(111) surface (red), with the first/second oxygen marked by solid/dashed lines. In the evaluation of the extraction of the second oxygen, the first oxygen has been removed from the one of the equivalent favored extraction sites at the Ce vacancy but not connected to Pd. The dotted lines are included as guides to the eye. Color in insert atomic model: red (O), blue (Pd), and beige (Ce). Data tabulated in Table S7 with identification number in insert atomic figure. (b) Pd-facilitated oxygen extraction energies (one O per nm^2) indicated by color scale via O(s) + CO(g) → CO_2(g) for the terrace site. (c) Corresponding data for the step site, starting from the stoichiometric PdO_2 surface. CO adsorption structures and energetics. (d) Thermodynamically favored Pd_1 state at various conditions.

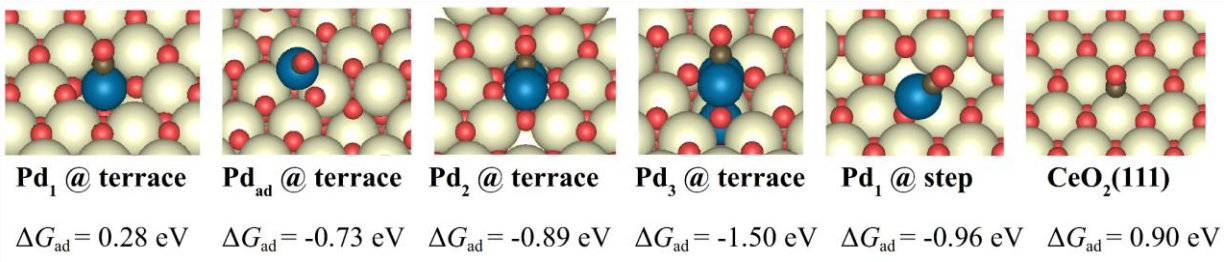

Supplementary Figure 29. Optimized structures and adsorption free energies at 25 ºC and 0.02 bar of CO(g) of adsorbed CO on different Pd/CeO_2 structures.

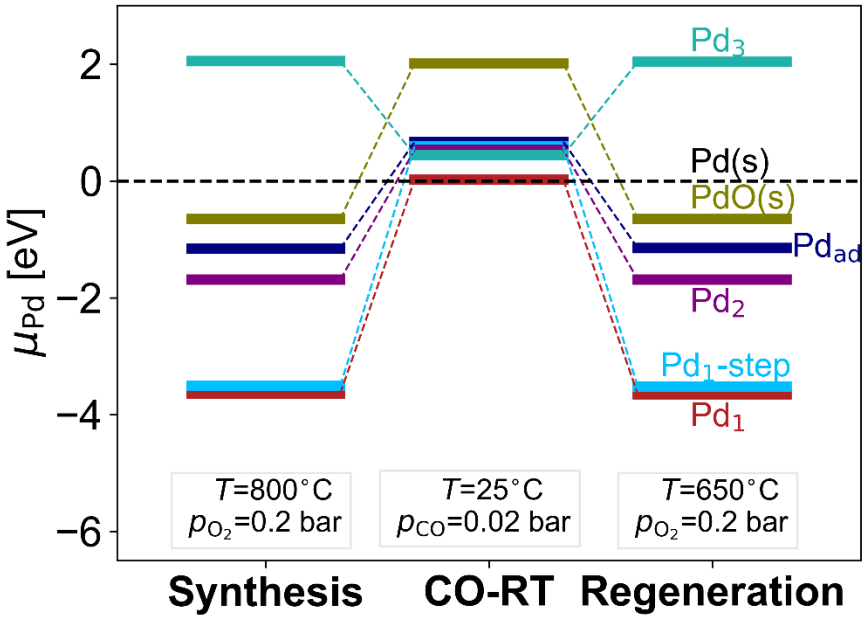

Supplementary Figure 30. Chemical potential of Pd (μ_{Pd}) relative Pd(s) in different states at different conditions computed from DFT energetics with thermodynamic corrections from NIST-JANAF database and vibrational analysis[25]. Pd at terrace model unless otherwise stated.

Supplementary Tables

Supplementary Table 1. Best fitting results of EXAFS at Pd K-edge for Pd foil, PdO/Al_2O_3, and Pd_1/CeO_2 in as-synthesized state and after different RT-CO and 275-CO treatments.

Samples	Scattering Pair	Coordination Number (error)	Debye-Waller Factor ($Å^2$)	E_0 (eV)	R/R_{Reff} (Å)	R factor
Pd foil	Pd-Pd	12.0	0.0056	3.2	2.740/2.745	0.0012
PdO/Al_2O_3	Pd-O	4.0	0.0019	0.108	2.017/2.010	0.0083
	Pd-Pd	8.0	0.0074		3.428/3.407	
	Pd-Pd	4.0	0.0064		3.048/3.020	
Pd_1/CeO_2	Pd-O	4.5 (± 0.5)	0.0022	-1.807	1.994/2.000	0.0127
	Pd-Ce	4.0 (± 0.4)	0.0077		3.171/3.200	
Pd_1/CeO_2_RT-CO/1min	Pd-O	3.6 (± 0.4)	0.0016	-3.69	1.988/2.000	0.0167
	Pd-Ce	4.0 (± 0.4)	0.0094		3.175/3.200	
Pd_1/CeO_2_RT-CO/5min	Pd-O	3.1 (± 0.3)	0.0016	-2.705	1.994/2.000	0.0113
	Pd-Ce	2.6 (± 0.3)	0.0076		3.183/3.200	
	Pd-Pd	1.0 (± 0.3)	0.0087		2.718/2.700	
Pd_1/CeO_2_275-CO	Pd-O	2.0	0.0019	-7.093	1.985/1.990	0.0214
	Pd-Pd	1.0	0.0050		3.289/3.290	
	Pd-Pd	4.0	0.0138		2.724/2.730	
Pd_1/CeO_2_spent	Pd-O	4.4 (± 0.4)	0.0017	-2.989	1.992/2.000	0.0158
	Pd-Ce	4.0 (± 0.5)	0.0082		3.180/3.200	

Fitting range for Pd_1/CeO_2 catalysts:
R space: 1.1-3.3 (Å); K space: 3 - 12 ($Å^{-1}$).

Note: Considering the ultrasmall size of the clusters, the Pd-Pd bond length is found to be shorter than the Pd-Pd bond length in the bulk PdO

Supplementary Table 2. Summary of the Brunauer–Emmett–Teller (BET) specific surface areas, Ea, and T50/T90 of Pd_1/CeO_2 and PdO/Al_2O_3 catalysts with different treatments, as well as under different conditions for CH_4 catalytic combustion.

Samples and treatments	BET (m^2/g)	Ea (kJ/mol)	T50 (^oC) dry	T90 (^oC) dry	T50 (^oC) 4.2% H_2O	T90 (^oC) 4.2% H_2O
Pd_1/CeO_2	45.5	65.8	615	731	_	_
Pd_1/CeO_2 _RT-CO/5min	47.1	89.8	303	345	373	410
Pd_1/CeO_2_275-CO	_	109.2	298	338	_	_
PdO/Al_2O_3	151.6	85.2	332	403	428	509

Supplementary Table 3. Summary of CH_4 oxidation over Pd-based catalysts, including reaction conditions, reaction rates, E_a and T50/T90 (temperatures required for 50/90 % CH_4 conversions) in CH_4 oxidation.[a]

No.	Pd Catalysts	Pd loading (wt. %)	Reaction gas (%)		GHSV (L/g-h)	Ea (kJ/mol)	Reaction rate ($mmol_{CH4}$ mol_{Pd}^{-1} s^{-1})	T50 (°C)	T90 (°C)	Ref.
			CH_4	O_2						
1	Pd_1/CeO_2	1 wt. % Pd	0.068	14	300	65.8	0.33[b] (300 °C)	615	731	this work
2	Pd_1/CeO_2 _RT-CO	1 wt. % Pd	0.068	14	300	89.8	11.8[b] (300 °C)	303	345	this work
3	PdO/Al_2O_3	1 wt. % Pd	0.068	14	300	85.2	5.8 (300 °C)	332	403	this work
4	$1Pd/2Pt@CeO_2$	1.1 wt. % Pd	0.068	14	300	74	3.3[c] (300 °C)	330	390	[35]
5	$1Pd/2Pt@CeO_2$	1.1 wt. % Pd	1	10	300	_	51[c] (300 °C)	_	_	[35]
6	$(1Pd+2Pt)/CeO_2$	1.1 wt. % Pd	0.068	14	300	80	0.91 (300 °C)	375	420	[35]
7	$Pd@CeO_2/H\text{-}Al_2O_3$	1 wt. % Pd	0.5	2	200	103	23.4 (250 °C)	305	350	[30]
8	Al_2O_3-$Pd/MgAl_2O_4$	1 wt. % Pd	0.5	10	40	_	10.4 (300 °C)	335	400	[36]
9	$LaFeO_3$-$Pd/MgAl_2O_4$	0.53 wt. % Pd	0.5	5	72	75	3.7 (300 °C)	_	_	[37]
10	Pd-Ce NW @SiO_2	1.5 wt. % Pd	1	21	36	100.4	9.65 (275 °C)	300	350	[38]
11	Pd/Na-MOR	1 wt. % Pd	1	4	70	75	4.33 (275 °C)	335	385	[39]
12	Pd-CeO_2-BM	0.8 wt. % Pd	0.5	2	200	_	22.1 (350 °C)	350	485	[40]
13	Pd/CeO_2-HHA	0.77 wt. % Pd	1	20	15	63	11.2 (300 °C)	300	335	[41]
14	Pd/CeO_2	1.8 wt. % Pd	1	21	30	_	2.6 (300 °C)	310	350	[42]
15	Pd/ZrO_2	1 wt. % Pd	0.1	3.15	240	_	2.0 (300 °C)	355	405	[43]

16	$NiO@PdO/Al_2O_3$	0.2 wt. % Pd	1	21	30	89	50 (300 °C)	320	375	[44]
17	PdO/CeO_2/SBA-15	1 wt. % Pd	0.1	10	180	_	1.3 (300 °C)	360	400	[45]
18	Pd/CeO2-SCS	1.7 wt. % Pd	0.5	2	200	169	2.9 (280 °C)	355	425	[46]
19	$PdAc/CeO_2$-DM	1 wt. % Pd	0.5	2	90	_	2.7 (250 °C)	325	375	[47]
20	Pd^{4+}/CeO_2 (111) [d]	PdO_x clusters partially embedded in CeO_2	–	–	–	115	–	–	–	[48]
21	Pd doped CeO_2 (111) [d]	Pd adopts a square planar configuration	–	–	–	80-110	–	–	–	[7]
22	Pd doped CeO_2 (111) [d]	two Pd^{2+} ions substitute one Ce^{4+} ion	–	–	–	101.3	–	–	–	[6]

[a] Values were reported in the references or extracted from the reported figures, e.g., calculation based on light-off curves.
[b] Reaction rates of as-synthesized and RT-CO activated Pd_1/CeO_2 catalysts were measured under low CH_4 conversions (< 20 %) by adjusting the GHSV.
[c] The reaction rate has been widely confirmed to show a positive (unit order) dependence on the partial pressure of CH_4 and a nearly zero order dependence on the partial pressure of O_2 [35,39].
[d] Computational studies which are not based on experimental results.

Supplementary Table 4. Thermodynamic data used for computing the chemical potential of the species in Fig. 4 and Fig. S30. All degrees of freedom accounted for regarding gas-phase molecules and the two topmost atomic layers for the adsorbates with reported values corresponding to the difference between the surface with and without the adsorbate.

				298 K			923 K			1073 K		
Species[a]	Fugacity	E_{ele}[b]	ZPE	$\int C_p\,dT$+ZPE	S	$\mu^{p\circ\rightarrow p}$	$\int C_p\,dT$+ZPE	S	$\mu^{p\circ\rightarrow p}$	$\int C_p\,dT$+ZPE	S	$\mu^{p\circ\rightarrow p}$
	(atm)	(eV)	(eV)	(eV)	(eV/K)	(eV)	(eV)	(eV/K)	(eV)	(eV)	(eV/K)	(eV)
Gas phase												
O_2	0.20	-9.19	0.10	0.19	2.13E-3	-0.04	0.39	2.50E-3	-0.13	0.45	2.55E-3	-0.15
CO	0.02	-15.31	0.13	0.22	2.05E-3	-0.10	0.42	2.41E-3	-0.31	0.47	2.46E-3	-0.36
CO_2	0.00	-22.86	0.31	0.41	2.22E-3	-0.18	0.71	2.76E-3	-0.55	0.79	2.84E-3	-0.64
Surface states												
$O_{surface}\,(CeO_2)$	n/a	-7.37	0.03	0.08	3.33E-4	n/a	0.24	6.22E-4	n/a	0.28	6.61E-4	n/a
$O_{ad}\,(CeO_2)$	n/a	-2.91	0.06	0.08	1.29E-4	n/a	0.17	2.88e-4	n/a	0.19	3.12E-4	n/a
Pd(s)	n/a	-5.22	0.02	0.06	2.47E-4	n/a	0.18	4.62E-4	n/a	0.21	4.91E-4	n/a
PdO(s)[c]	n/a	-6.19	0.06	0.06	-8.24E-4	n/a	0.17	-6.24E-4	n/a	0.20	-5.94E-4	n/a
Pd_{ad}^{2+}(ts)	n/a	-6.39	0.10	0.12	3.10E-4	n/a	0.18	4.16E-4	n/a	0.21	4.39E-4	n/a
$Pd_{ad}^{\delta+}$(ts)	n/a	-3.57	0.10	0.12	3.10E-4	n/a	0.18	4.16E-4	n/a	0.21	4.39E-4	n/a
Pd_1^{2+}(ts)	n/a	-8.95	0.10	0.12	1.92E-4	n/a	0.26	4.21E-4	n/a	0.29	4.57E-4	n/a
$Pd_1^{\delta+}$(ts)	n/a	-5.98	0.10	0.12	1.92E-4	n/a	0.26	4.21E-4	n/a	0.29	4.57E-4	n/a
Pd_1^{2+}(ss)	n/a	-8.87	0.10	0.12	1.92E-4	n/a	0.26	4.21E-4	n/a	0.29	4.57E-4	n/a
$Pd_1^{\delta+}$(ss)	n/a	-3.96	0.10	0.12	1.92E-4	n/a	0.26	4.21E-4	n/a	0.29	4.57E-4	n/a
Pd_2^{2+}(ts)	n/a	-7.01	0.08	0.10	9.80E-5	n/a	0.25	3.56E-4	n/a	0.28	3.94E-4	n/a

$Pd_2^{\delta+}$(ts)	n/a	-3.85	0.08	0.10	9.80E-5	n/a	0.25	3.56E-4	n/a	0.28	3.94E-4	n/a
Pd_3^{2+}(ts)	n/a	-3.15	0.02	0.08	4.44E-4	n/a	0.24	7.33E-4	n/a	0.28	7.72E-4	n/a
$Pd_3^{\delta+}$(ts)	n/a	-2.61	0.02	0.08	4.44E-4	n/a	0.24	7.33E-4	n/a	0.28	7.72E-4	n/a
CO*@CeO_2	n/a	-14.98	0.17	0.24	5.28E-4	n/a	0.46	9.24E-4	n/a	0.52	9.82E-4	n/a
CO*@$Pd_{ad}^{\delta+}$(ts)	n/a	-16.64	0.21	0.28	5.44E-4	n/a	0.54	1.01E-3	n/a	0.61	1.09E-3	n/a
2CO*@$Pd_{ad}^{\delta+}$(ts)	n/a	-15.77	0.21	0.28	5.44E-4	n/a	0.54	1.01E-3	n/a	0.61	1.09E-3	n/a
CO*@$Pd_1^{\delta+}$(ts)	n/a	-15.65	0.22	0.28	5.06E-4	n/a	0.54	9.69E-4	n/a	0.61	1.04E-3	n/a
CO*@$Pd_1^{\delta+}$(ss)	n/a	-16.87	0.21	0.28	5.44E-4	n/a	0.54	1.01E-3	n/a	0.61	1.09E-3	n/a
CO*@$Pd_2^{\delta+}$(ts)	n/a	-16.76	0.08	0.10	9.80E-5	n/a	0.25	3.56E-4	n/a	0.28	3.94E-4	n/a
CO*@$Pd_3^{\delta+}$(ts)	n/a	-17.39	0.21	0.28	5.28E-4	n/a	0.54	9.95E-4	n/a	0.61	1.07E-3	n/a

[a] (ts) = terrace site, (ss) = step site, δ+ indicate here that two oxygen atoms have been extracted per nm^2.
[b] Including gas-phase corrections, see methods section.
[c] Thermochemical values obtained by subtracting $0.5O_2$(g) from those of PdO(s).

Supplementary Table 5. Geometrical details of the DFT-identified low energy Pd_1 and Pd_2 structures at the terrace and step surface models. EXAFS data included for comparison.

Structure	Bond	@CeO_2(111) [Å]	@CeO_2-step [Å]	EXAFS [Å]
Pd_1O_4	*Pd(1)-O(1)*	1.95 (2.03)[a]	2.02 (2.02)[a]	1.99 ± 0.01
	Pd(1)-O(2)	1.97 (2.00)[a]	1.89 (2.00)[a]	1.99
	Pd(1)-O(3)	1.97 (2.01)[a]	1.89 (2.04)[a]	1.99
	Pd(1)-O(4)	1.89 (2.03)[a]	1.97 (2.03)[a]	1.99
	Pd(1)-Ce(1)	3.29 (3.17)[a]	3.30 (2.98)[a]	3.17 ± 0.01
	Pd(1)-Ce(2)	3.29 (3.20)[a]	3.30 (3.09)[a]	3.17
	Pd(1)-Ce(3)	3.27 (3.14)[a]	3.25 (3.17)[a]	3.17
	Pd(1)-Ce(4)	3.27 (3.14)[a]	3.25 (3.18)[a]	3.17
Pd_2O_7	*Pd(1)-O(1)*	2.03	2.05	1.99 ± 0.01
	Pd(1)-O(2)	1.99	1.95	1.99
	Pd(1)-O(3)	1.99	2.01	1.99
	Pd(1)-O(4)	2.01	2.03	1.99
	Pd(2)-O(5)[b]	1.99	2.01	1.99
	Pd(2)-O(6)	2.02	2.03	1.99
	Pd(2)-O(7)	2.02	2.02	1.99
	Pd(1)-Ce(1)	3.16	3.27	3.18 ± 0.01
	Pd(1)-Ce(2)[c]	3.16	3.26	3.18
	Pd(1)-Ce(3)	3.11	3.20	3.18
	Pd(1)-Ce(4)[c]	3.11	3.17	3.18
	Pd(2)-Ce(5)	3.13	3.40	3.18
	Pd(2)-Ce(6)	3.13	3.32	3.18
	Pd(1)-Pd(2)	2.77	3.89	2.72

[a] Values in parenthesis for a moderately reduced CeO_2 surface with one O vacancy at close proximity to Pd (one of the O atoms that used to be bonded to Ce at the site that Pd now occupies). [b] For the Pd_2O_7@CeO_2-step model, O(5)=O(3) and [c] Ce(2) and Ce(4) are shared between the Pd atoms.

Supplementary Table 6. Computed oxygen vacancy (V_O) energies for the terrace surface models presented in Fig. S28.A-B, i.e., energies are relative CO(g) + O* → CO_2(g).

Identifier	**Distance to Pd_1 [Å]**	**$\Delta G(V_O\text{-}1^{st})$ [eV]**	**$\Delta G(V_O\text{-}2^{nd})$ [eV]**
Pristine CeO_2(111)	n/a	-0.20	-0.12
Pd_1 @ CeO_2(111):			
Site 1	7.54	-2.29	-0.14
Site 2	7.97	-2.31	-0.14
Site 3	6.39	-2.22	-0.24
Site 4	6.90	-2.34	-0.28
Site 5	7.54	-2.29	0.06
Site 6	4.34	-2.45	-0.17
Site 7	3.73	-3.31	n/a[a]
Site 8	5.73	-2.57[b]	-0.33
Site 9	5.16	-2.13	-0.11
Site 10	1.89	-1.44[c]	0.20
Site 11	3.72	-3.31	-1.18
Site 12	6.90	-2.34	-0.24
Site 13	5.16	-2.13	-0.03
Site 14	4.34	-2.45	-0.30
Site 15	6.39	-2.22	-0.05
Site 16	8.00	-2.14	-0.34
Site A	3.44	-2.62[c]	Not included
Site B	3.43	-3.10[b]	Not included

[a] This oxygen is the first to be extracted and not available for the extraction of the second oxygen.
[b] The subsurface B atom was constrained in the lateral dimensions to evaluate the energy of site 8, the energy for site B corresponds to the unconstrained calculation.
[c] The subsurface A atom was constrained in the lateral dimensions to evaluate the energy of site 10, the energy for site A corresponds to the unconstrained calculation.

Supplementary Table 7. Computed oxygen vacancy (V_O) energies for the stepped surface models presented in Fig. S28.C and for further surface reduction. All energies are relative $CO(g)+O^*->CO_2(g)$.

Identifier [a]	**$\Delta G(V_O\text{-}1^{st})$** [b] **[eV]**	**$\Delta G(V_O\text{-}2^{nd})$ [eV]**	**$\Delta G(V_O\text{-}3^{rd})$ [eV]**	**$\Delta G(V_O\text{-}4^{th})$ [eV]**
Stepped $CeO_2(111)$	-1.33 (at edge)	-0.16 (at edge)	0.86 (at edge)	Not tested
Pd_1 @ $CeO_2(111)$ step:				
Perimeter (at Pd_1)	-3.07	-2.49[c]	n/a[d]	n/a[d]
Edge (at Pd_1)	-2.34	-0.72	-0.40	Not tested
Edge (near Pd_1)	-3.56	-0.96	-1.95	-0.38
Sub edge (at Pd_1)	-1.80	-0.50	0.20	Not tested
Sub edge (near Pd_1)	-1.53	-0.81	0.12	Not tested
Terrace (above step)	-2.21	-1.00	-0.84	Not tested
Terrace (below step)	-2.03	-0.90	-1.13	Not tested

[a] The lowest energy position is picked if two unique sites of the same category exist due to symmetry breaking resulting from the creation of the oxygen vacancy, V_O.
[b] This column contains V_O relative to the stoichiometric surface with adsorbed PdO_2, the thermodynamically favored state at synthesis conditions is 'Edge (near Pd)'. For the surface without Pd, the reference state (i.e., 0 V_O) has 2 O_{ad} pre-adsorbed per unit cell (same number of O as for PdO_2).
[c] Leads to the rearrangement of surface O to heal the V_O edge site generating a Pd_1O_2 structure with two V_O at the perimeter (at Pd_1) sites. [d] All oxygen at this site has already been extracted.

Supplementary Table 8. Stepwise Gibbs free energy of O vacancy (V_O) formation and oxygen adsorption (O_{ad}) described by $CO(g) + O_{surface/ad} \leftrightarrow CO_2(g)$ at 298.15 K, p_{CO} = 0.02 bar, and p_{CO2} = 0.001 bar for the considered Pd structures on the $CeO_2(111)$ terrace and step models (relative surface terminations at synthesis conditions; stoichiometric for $CeO_2(111)$ terrace and V_{Ce} for PdO_x on the terrace model, as well as stoichiometric for CeO_2 step and $Pd_{ad}+2O_{ad}$ for PdO_x on the step model).

		$CeO_2(111)$ model		Step-II model	
Structure	**$\pm n_O$**	**$\Delta G(V_O)$[a] [eV]**	**$\Delta G(O_{ad})$[b] [eV]**	**$\Delta G(V_O)$[a] [eV]**	**$\Delta G(O_{ad})$[b] [eV]**
CeO_2	1	-0.20	4.63 (2.03)[d]	0.88	3.27 (0.67)[d]
Pd_1	1	-3.31	0.56 (-2.04)[d]	-1.67	3.69 (1.09)[d]
	2	-1.18	n/a[c]	-0.18	n/a[c]
	3	0.44	n/a[c]	-0.53	n/a[c]
Pd_{ad}	1	-2.85	2.78 (0.18)[d]	n/a[c]	n/a[c]
	2	-1.58	n/a[c]	n/a[c]	n/a[c]
	3	-0.41	n/a[c]	n/a[c]	n/a[c]
Pd_2	1	-0.90	2.60 (0.00)[d]	0.91	1.37 (-1.23)
	2	-0.23	n/a[c]	n/a[c]	n/a[c]
	3	0.53	n/a[c]	n/a[c]	n/a[c]
Pd_3	1	-0.75	0.72 (-1.88)[d]	n/a[c]	n/a[c]
	2	0.17	n/a[c]	n/a[c]	n/a[c]
	3	n/a[c]	n/a[c]	n/a[c]	n/a[c]

[a] Relative to surface with n+1 $O_{surface}$.
[b] relative to surface with n-1 O_{ad}.
[c] Not applicable or not tested as previous results indicate a thermodynamically inaccessible state.
[d] With $0.5O_2 \rightarrow O_{ad}$ as reference (p_{O2}=0.2 bar).

Supplementary References

1 Ravel, B. & Newville, M. ATHENA, ARTEMIS, HEPHAESTUS: data analysis for X-ray absorption spectroscopy using IFEFFIT. *J. Synchrotron Rad.* **12**, 537-541 (2005).

2 Hjorth Larsen, A. *et al.* The atomic simulation environment—a Python library for working with atoms. *Journal of Physics: Condensed Matter* **29**, 273002, (2017).

3 Jones, J. *et al.* Thermally stable single-atom platinum-on-ceria catalysts via atom trapping. *Science* **353**, 150-154 (2016).

4 Branda, M. M., Ferullo, R. M., Causà, M. & Illas, F. Relative stabilities of low index and stepped CeO_2 surfaces from hybrid and GGA + U implementations of density functional theory. *J. Phys. Chem. C* **115**, 3716-3721 (2011).

5 Matz, O. & Calatayud, M. Breaking H_2 with CeO_2: effect of surface termination. *ACS Omega* **3**, 16063-16073 (2018).

6 Su, Y., Liu, J.-X., Filot, I. A., Zhang, L. & Hensen, E. J. Highly active and stable CH4 oxidation by substitution of Ce^{4+} by two Pd^{2+} ions in CeO_2 (111). *ACS Catal.* **8**, 6552-6559 (2018).

7 Su, Y.-Q., Filot, I. A., Liu, J.-X. & Hensen, E. J. Stable Pd-doped ceria structures for CH_4 activation and CO oxidation *ACS Catalysis* **8**, 75-80 (2017).

8 Tang, W. *et al.* Methane complete and partial oxidation catalyzed by Pt-doped CeO_2. *J. Catal.* **273**, 125-137 (2010).

9 Dvořák, F. *et al.* Creating single-atom Pt-ceria catalysts by surface step decoration. *Nat. Commun.* **7**, 10801, (2016).

10 Nguyen, P. T. *et al.* Rational development of Co-doped mesoporous ceria with high peroxidase-mimicking activity at neutral pH for paper-based colorimetric detection of multiple biomarkers. *Adv. Funct. Mater.* **32**, 2112428, (2022).

11 Kümmerle, E. A. & Heger, G. The Structures of C–$Ce_2O_{3+\delta}$, Ce_7O_{12}, and $Ce_{11}O_{20}$. *J. Solid State Chem.* **147**, 485-500 (1999).

12 Kunwar, D. *et al.* Stabilizing high metal loadings of thermally stable platinum single atoms on an industrial catalyst support. *ACS Catal.* **9**, 3978-3990 (2019).

13 Kozlov, S. M., Viñes, F., Nilius, N., Shaikhutdinov, S. & Neyman, K. M. Absolute surface step energies: accurate theoretical methods applied to ceria nanoislands. *J. Phys. Chem. Lett.* **3**, 1956-1961 (2012).

14 Liu, J.-C., Wang, Y.-G. & Li, J. Toward rational design of oxide-supported single-atom catalysts: atomic dispersion of gold on ceria. *J. Am. Chem. Soc.* **139**, 6190-6199 (2017).

15 Lu, Y. *et al.* Unraveling the intermediate reaction complexes and critical role of support-derived oxygen atoms in CO oxidation on single-atom Pt/CeO_2. *ACS Catal.* **11**, 8701-8715 (2021).

16 Kresse, G. & Hafner, J. Ab initio molecular dynamics for liquid metals. *Phys. Rev. B* **47**, 558-561 (1993).

17 Kresse, G. & Furthmüller, J. Efficient iterative schemes for ab initio total-energy calculations using a plane-wave basis set. *Physical Review B* **54**, 11169-11186, doi:10.1103/PhysRevB.54.11169 (1996).

18 Perdew, J. P., Burke, K. & Ernzerhof, M. Generalized gradient approximation made simple. *Phys. Rev. Lett.* **77**, 3865-3868 (1996).

19 Dudarev, S. L., Botton, G. A., Savrasov, S. Y., Humphreys, C. J. & Sutton, A. P. Electron-energy-loss spectra and the structural stability of nickel oxide: An LSDA+U study. *Phys. Rev. B* **57**, 1505-1509 (1998).
20 Fabris, S., de Gironcoli, S., Baroni, S., Vicario, G. & Balducci, G. Taming multiple valency with density functionals: A case study of defective ceria. *Phys. Rev. B* **71**, 041102, (2005).
21 Kresse, G. & Joubert, D. From ultrasoft pseudopotentials to the projector augmented-wave method. *Phys. Rev. B* **59**, 1758-1775 (1999).
22 Blöchl, P. E. Projector augmented-wave method. *Phys. Rev. B* **50**, 17953-17979 (1994).
23 Monkhorst, H. J. & Pack, J. D. Special points for Brillouin-zone integrations. *Phys. Rev. B* **13**, 5188-5192 (1976).
24 Peterson, A. A., Abild-Pedersen, F., Studt, F., Rossmeisl, J. & Nørskov, J. K. How copper catalyzes the electroreduction of carbon dioxide into hydrocarbon fuels. *Energy Environ. Sci.* **3**, 1311-1315 (2010).
25 Chase, M. W. NIST-JANAF Thermochemical Tables, 4th Edition. *J. Phys. Chem. Ref. Data* (1998).
26 Wang, V., Xu, N., Liu, J.-C., Tang, G. & Geng, W.-T. VASPKIT: A user-friendly interface facilitating high-throughput computing and analysis using VASP code. *Comput. Phys. Commun.* **267**, 108033, (2021).
27 Jiang, D. *et al.* Elucidation of the active sites in single-atom Pd_1/CeO_2 catalysts for low-temperature CO oxidation. *ACS Catal.* **10**, 11356-11364 (2020).
28 Weilenmann, M. F., Soltic, P. & Hausberger, S. The cold start emissions of light-duty-vehicle fleets: A simplified physics-based model for the estimation of CO_2 and pollutants. *Sci. Total Environ.* **444**, 161-176 (2013).
29 Smit, R. & Ntziachristos, L. *Cold start emission modelling for the Australian petrol fleet*. Vol. 47 (Clean Air Society of Australia & New Zealand, 2013).
30 Cargnello, M. *et al.* Exceptional activity for methane combustion over modular $Pd@CeO_2$ subunits on functionalized Al_2O_3. *Science* **337**, 713-717 (2012).
31 Alcala, R. *et al.* Atomically dispersed dopants for stabilizing ceria surface area. *Appl. Catal. B: Environ.* **284**, 119722, (2021).
32 Pereira-Hernández, X. I. *et al.* Tuning $Pt\text{-}CeO_2$ interactions by high-temperature vapor-phase synthesis for improved reducibility of lattice oxygen. *Nat. Commun.* **10**, 1358 (2019).
33 Yu, W.-Z. *et al.* Construction of active site in a sintered copper–ceria nanorod catalyst. *J. Am. Chem. Soc.* **141**, 17548-17557 (2019).
34 Muravev, V. *et al.* Interface dynamics of $Pd–CeO_2$ single-atom catalysts during CO oxidation. *Nat. Catal.* **4**, 469–478 (2021).
35 Xiong, H. *et al.* Engineering catalyst supports to stabilize PdO_x two-dimensional rafts for water-tolerant methane oxidation. *Nat. Catal.* **4**, 830-839 (2021).
36 Yang, J. *et al.* A hydrothermally stable irreducible oxide ‐ modified $Pd/MgAl_2O_4$ catalyst for methane combustion. *Angew. Chem. Int. Ed.* **132**, 18680-18684 (2020).
37 Onn, T. M. *et al.* Smart Pd catalyst with improved thermal stability supported on high-surface-area $LaFeO_3$ prepared by atomic layer deposition. *J. Am. Chem. Soc.* **140**, 4841-4848 (2018).
38 Peng, H. *et al.* Confined ultrathin Pd-Ce nanowires with outstanding moisture- and SO_2-tolerance in methane combustion. *Angew. Chem. Int. Ed.* **57**, 8953-8957 (2018).
39 Petrov, A. W. *et al.* Stable complete methane oxidation over palladium based zeolite catalysts. *Nat. Commun.* **9**, 2545 (2018).

40 Danielis, M. *et al.* Outstanding methane oxidation performance of Pd-embedded ceria catalysts prepared by a one-step dry ball-milling method. *Angew. Chem. Int. Ed.* **57**, 10212-10216 (2018).
41 Ma, J. *et al.* The relationship between the chemical state of Pd species and the catalytic activity for methane combustion on Pd/CeO_2. *Catal. Sci. Technol.* **8**, 2567-2577 (2018).
42 Lei, Y. *et al.* Typical crystal face effects of different morphology ceria on the activity of Pd/CeO_2 catalysts for lean methane combustion. *Fuel* **233**, 10-20 (2018).
43 Hong, E., Kim, C., Lim, D.-H., Cho, H.-J. & Shin, C.-H. Catalytic methane combustion over Pd/ZrO_2 catalysts: Effects of crystalline structure and textural properties. *Appl. Catal. B: Environ.* **232**, 544-552 (2018).
44 Zou, X., Rui, Z. & Ji, H. Core–shell NiO@PdO nanoparticles supported on alumina as an advanced catalyst for methane oxidation. *ACS Catal.* **7**, 1615-1625 (2017).
45 Dai, Y. *et al.* Mesoporous silica-supported nanostructured PdO/CeO_2 catalysts for low-temperature methane oxidation. *ACS Appl. Mater. Interfaces* **10**, 477-487 (2017).
46 Colussi, S. *et al.* Nanofaceted Pd-O sites in Pd-Ce surface superstructures: enhanced activity in catalytic combustion of methane. *Angew. Chem. Int. Ed* **48**, 8481-8484 (2009).
47 Danielis, M. *et al.* Methane oxidation activity and nanoscale characterization of Pd/CeO2 catalysts prepared by dry milling Pd acetate and ceria. *Appl. Catal. B: Environ.* **282**, 119567, (2021).
48 Senftle, T. P., Van Duin, A. C. & Janik, M. J. Role of site stability in methane activation on $Pd_xCe_{1-x}O_\delta$ surfaces. *ACS Catal.* **5**, 6187-6199 (2015).